Radboud University Nijmegen

Faculty of Science

Tidal resonances in extreme mass ratio inspirals

Investigating the behavior of static and dynamic tidal resonances

Master thesis Physics & Astronomy

Supervisor:
dr. Béatrice Bonga

Author:
Bram ten Brink

Second reader:
prof. dr. Badri Krishnan

August 2025

Abstract

With the anticipated launch of the Laser Interferometer Space Antenna (LISA) in about a decade from now, the focus of gravitational wave astronomy is shifting partially from the Hz-kHz range of current ground-based detectors to the mHz range, which can be probed when LISA becomes operational. One of the main classes of new sources that can be observed with LISA are extreme mass ratio inspirals (EMRIs), which are binaries with a very small mass ratio. The dynamics of these systems, and thus their emitted gravitational waves, can change in multiple ways in the presence of other stellar-mass bodies. One of the effects that external masses can induce are tidal resonances. If tidal resonances are not correctly modeled into gravitational waveforms of EMRIs, the LISA signal could be interpreted incorrectly. Either leading to wrong black hole parameter estimations, which could lead to wrong conclusions about underlying physics, or leading to the signal completely being missed all together. A semi-analytical framework has been developed to study the effects of tidal resonances in EMRIs. This work uses this framework to map and characterize the most relevant tidal resonances considering a single stationary compact external mass, and to estimate their induced jumps, providing fitting formulas that can be used to model these resonances into waveforms. It also highlights the complexities that arise when the external mass is allowed to move on a constrained circular orbit, laying the groundwork for future investigation.

Contents

1 Introduction

1.1 Gravitational waves

Einstein's general theory of relativity (GR) is one of the most important and well-supported theories in modern astrophysics [1]. The theory remains unchanged after more than a hundred years and has predicted phenomena like gravitational lensing, black holes (BHs) and gravitational waves (GWs). These phenomena have been tested experimentally. The effects of gravitational lensing were measured experimentally in 1919 [2], the first image of a black hole was presented in 2019 [3] and the first direct detection of GWs was presented in 2016 [4]. This first measurement of the GWs from a binary black hole merger by the LIGO detector can be seen as the start of gravitational wave astronomy. Since then, ground-based detectors have observed numerous GW events coming mostly from BH-BH mergers, but also from BH-neutron star (NS) and NS-NS mergers [5].

The next generation of GW detectors consists of two detector types: ground-based detectors and space-based detectors. Ground-based detectors like the Einstein Telescope (ET) and Cosmic Explorer (CE) will operate in the 1 Hz − 10 kHz range. As can be seen in figure 1, this is the same frequency band as the current ground based detectors like LIGO, Virgo and KAGRA. ET and CE will have higher sensitivity than current detectors allowing for more, and more precise detections [6]. The space-based detectors like Taiji, TianQin and the Laser Interferometer Space Antenna (LISA) will operate in the mHz range. This new frequency band allows researchers to detect new types of events like galactic white-dwarf binaries, binary massive black hole (MBH) mergers and extreme mass ratio inspirals (EMRIs) [6]. The sensitivity curves of LISA and TianQin are also shown in figure 1.

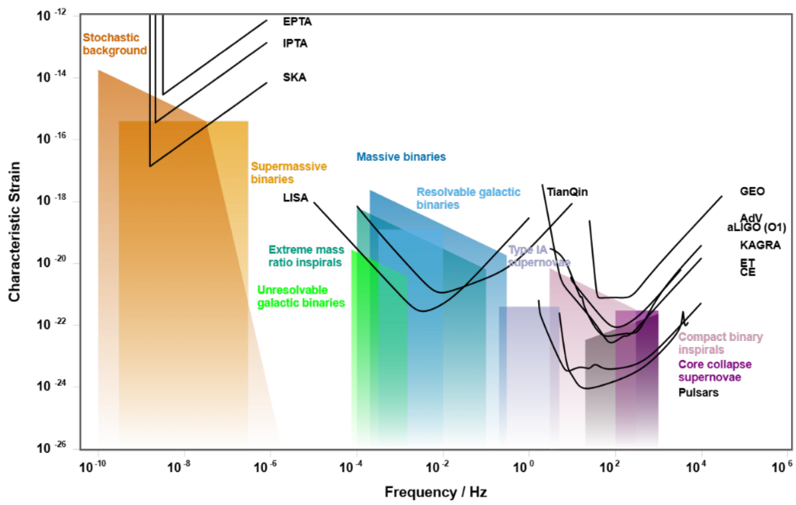

Figure 1: Graph showing the sensitivity curves of multiple detectors. The black lines indicate the minimal characteristic strain required for a GW to be detectable at a certain frequency. On the left the sensitivity curves of various pulsar timing arrays are shown, the sensitivity curve of LISA is shown in the middle and the sensitivity curves of the ground based detectors are shown on the right. The colored areas represent the frequency bands of various sources that can possibly be detected by the respective detectors. Source: gwplotter.com and [6].

These new space-based detectors come with new challenges in the analysis of the GW signal. GW information gathering makes use of matched filtering analysis, where the detector output is matched with a GW waveform template to extract information from the signal. It is expected that a detector like LISA will measure a large amount of sources at once. Some of these sources will not be resolvable and will act as noise to the detector. For the other sources, very accurate matched filtering techniques will be required to be able to resolve them from the GW signal. That is why accurate waveform templates will be needed. Creating these waveform templates requires accurate description of the dynamics of the system, so accurate models of the potential measurable sources is crucial.

1.2 Extreme mass ratio inspirals

One of the main groups of potentially measurable GW sources of LISA is EMRIs [7]. An EMRI is a binary that consists of a supermassive ($\sim 10^5 - 10^7 M_\odot$) BH (SMBH) and a compact stellar-mass ($\sim 1 - 100 M_\odot$) object [8]. The large difference in masses results in a very small mass ratio $\eta = \frac{M_2}{M_1}$, where M_1 is the mass of the supermassive BH and M_2 is the mass of the stellar-mass object.

A lot is still unknown about the formation of EMRIs. The most well-known way is via scattering and capture processes [8]. This usually involves a stellar-mass object approaching very close to the SMBH. Since tidal forces at these distances are very strong, the stellar-mass object has to be compact in order to keep its shape and not be pulled apart [9]. This close approach induces a large loss of orbital energy due to gravitational radiation. As a result the compact object gets 'trapped' around the SMBH. This channel seems to produce mostly eccentric inspirals. There are other possible channels through which EMRIs are formed such as tidal disruption events or wet EMRI formation [10]. Some of these other channels can be just as (or more) important as the traditional 'main' channel [10]. These channels will not be discussed, however.

Because of the small mass ratio, the inspiral of the binary is slow. Resulting in the emission of low frequency ($\sim 10^{-2}$ Hz) GWs [11] and a large amount ($\sim 10^5$) of cycles [8] spent in the measurable band of space-based detectors. This will allow researchers to probe the inspiral for a very long time and thus probe the spacetime very well, which allows for high precision test of GR. An example of these tests could be checking if these 'black holes' are really Kerr BHs and not something else. EMRI GW signals can also give extremely accurate measurements of physical parameters like BH spins and masses (up to an accuracy of $\sim 0.001\%$ compared to current accuracies of $\sim 10\%$!), which could give information about cosmology and the evolution of massive BHs [9].

The small parameter η allows for a perturbative description of the EMRI. At lowest order, the stellar-mass object can be described as a massless test particle moving in the spacetime of the SMBH. This means that the dynamics of the stellar-mass object can be described with Kerr geodesics. These Kerr orbits carry three characteristic frequencies: the radial (ω_r), azimuthal (ω_θ) and polar (ω_ϕ) frequencies. At higher orders in η, the mass of the stellar-mass object has to be taken into account. A 'self force' is introduced to model for the gravitational perturbation of the smaller mass, which determines how the orbit of the stellar-mass object deviates from the Kerr geodesics [8].

1.3 Resonances

Modeling this self force can be quite a challenge. In this case, the radiation reaction can be approximated as an adiabatic process. Here, it is assumed that the radiation reaction timescale τ_{rad} is much larger than the orbital timescale τ_{orb}: $\frac{\tau_{orb}}{\tau_{rad}} \sim \eta$[12]. The self force that appears at next-to-lowest order in the mass ratio expansion around Kerr can be separated into two parts. The dissipative part of the self force drives the inspiral. The contribution of this part of the force can accumulate over many orbits and thus have direct noticeable effects.

The conservative part can contribute to the small object's inertia. The contribution of this part does not accumulate secularly, however. This means that in the adiabatic approximation, where these contributions are usually averaged over many orbits, the conservative part rarely contributes[12]. One of the main exceptions to the last statement are resonances. A self force resonance happens when the radial and the azimuthal frequency become commensurate, i.e., $n\omega_r + k\omega_\theta = 0$ for any set of integers (n, k).

Generally, EMRIs are not isolated systems and are influenced by their surroundings. For example, an external object like a third body could exert a tidal force on the system. If this force is small enough, it can act on the EMRI in a similar way as the self force. The big difference being that the tidal force is a purely conservative force[8]. Meaning that, at leading order, the tidal force does not contribute to the orbit of M_2 except for resonances. Two types of tidal perturbations are considered in this thesis. The 'static' case considers a stationary perturber with mass M_*. The 'dynamic' case considers a perturber that is slowly moving around the central BH with fixed azimuthal frequency $\Omega_{\phi,\mathrm{td}} \ll \omega_\phi$. Figure 2 shows a schematic of the relevant situation. When a tidal resonance is encountered, in the case of a static perturber, we now have $n\omega_r + k\omega_\theta + m\omega_\phi = 0$ for any set of integers (n, k, m). For a dynamic perturber, a resonance occurs when $n\omega_r + k\omega_\theta + m\omega_\phi + s\Omega_{\phi,\mathrm{td}} = 0$ for any set of integers (n, k, m, s).

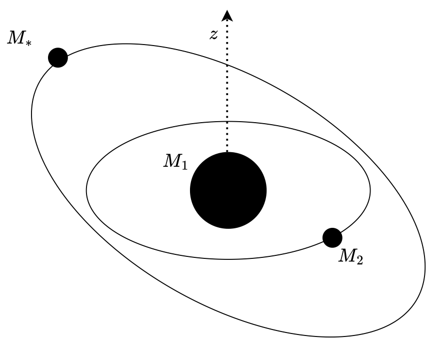

Figure 2: Schematic of the considered EMRI with tidal perturber M_*. M_1 and M_2 indicate the large BH mass and the compact object's mass, respectively. The perturber is always significantly further away from the central BH and can be stationary or slowly moving in a fixed circular orbit around M_1.

Resonances can induce shifts in the constants of motion, which in turn cause shifts in the orbital frequencies. In this thesis, the assumption is made that the tidal force is not extremely strong. Meaning that the evolution of the orbital frequencies is still dominated by the energy loss induced by dissipative part of the self force, i.e., all resonances are transient. The shifts in the orbital frequencies induced by resonances cause dephasing of the gravitational waveform. Since the matched filtering methods used for GW observation are very sensitive to the GW phase, it is important to model these resonances accurately.

1.4 Project overview

A semi-analytical method has been developed to study the effects of tidal resonances in EMRIs. The aim of this thesis is, for both the stationary and the dynamic configuration, to use this semi-analytical method to identify the most important tidal resonances, and calculate the shifts (ΔC) in the orbital constant induced by these resonances. A Mathematica code is used to calculate when these resonances happen and their shifts in E, L_z and Q for many different types of orbits. The data generated by this code is analyzed and processed so that it can be used in waveform codes like the open source FastEMRIWaveforms Python package [13].

Section 2 covers the main theoretical concepts needed for the calculation of the shifts or 'jumps' ΔC. This section starts off describing the metric perturbation induced by M_*. Details on the nature of the perturber will be specified to motivate the functional form of this perturbation. Then, a brief summary on Kerr geodesics will be presented. This part also introduces the relevant parameter space for the classification of orbits, together with the orbital frequencies. These frequencies will be used in the next part, where the resonance condition is derived. The last part of this section discusses the calculation of the jump amplitudes, and how they can be related to the jumps ΔC.

Section 3 discusses the main parts of the code that is used for the calculation of the location of the resonances and their jumps. The methods to solve the resonance condition will be covered, together with some ways to improve this part of the code. A short overview of the steps taken in the code to calculate the jump amplitudes is also given. This section ends with a discussion of the relevant parameter space for this project, together with the construction of the grid spanning this parameter space. The code will be used on the points of this grid.

The first part of the results in this thesis are shown in section 4. This section covers the selection procedure of the relevant resonances. The bulk of this section discusses the results of solving the resonance condition on the grid for the relevant resonances, which are shown in the form of resonance contours. The behavior of these resonance contours at different parts in the parameter space is discussed, and the results are compared to results of previous work. This section ends with a discussion of the difficulties that arise for the resonance contours of the dynamic case.

Section 5 contains the results and discussion of the jump amplitudes in the orbital constants. The first part covers the calculated data itself and highlights the most important patterns. A fitting procedure is applied to the data to obtain fitting formulas. The second part of this section discusses these fitting formulas and attempts to highlight the main problems with this fitting procedure, together with some potential ways to improve it. A summary and outlook are given in section 6.

2 Background

This section will describe the theoretical framework that is used to describe tidal resonances. After the introduction of some conventions and a short overview of the considered system, the induced metric perturbation will be discussed. Then, a short overview of Kerr geodesics is given. This section ends with a summary of the derivation of the resonance condition and the averaging integral used to compute the jump amplitudes in the orbital constants.

2.1 Conventions

Geometric units will be used in this thesis, so the speed of light in vacuum c and the gravitational constant G are set to 1. The mostly plus convention $(-,+,+,+)$ is used for all metrics. Greek indices represent all spacetime coordinates and range from 0 to 3. Lower case Latin indices represent spatial coordinates and range from 1 to 3, and upper case Latin indices represent angular coordinates only. The Einstein summation convention will be implied everywhere in this thesis.

In this project, an EMRI will be considered with a perturber. Figure 3 shows a schematic of the situation. The SMBH has mass M_1 and the secondary's mass is denoted as M_2. The perturber is assumed to be a compact object with mass M_* at a distance b from the SMBH. The EMRI has a mass ratio $\eta = \frac{M_2}{M_1}$. Two cases will be considered in this thesis: the stationary case, where the perturber is stationary, and the dynamic case, where the perturber is allowed to move in a circular orbit at a fixed speed. M_* is allowed to be at an arbitrary sky position in both cases. The inclination angles describing the sky location of the perturber are θ_y and θ_z, which correspond to the inclination from the equatorial plane and the angle with respect to the x-axis, respectively.

2.2 The metric perturbation

This subsection discusses the metric perturbation induced by M_*. Black hole perturbation theory is used to obtain the full perturbed metric, which is defined as

$$\tilde{g}_{\mu\nu} = g_{\mu\nu} + h_{\mu\nu}. \tag{1}$$

Here, $h_{\mu\nu}$ is the metric perturbation and $g_{\mu\nu}$ is the unperturbed metric of the background spacetime. The gravitational influence of M_2 will be ignored in this subsection and the background spacetime will be the Kerr spacetime of the central BH. The line element of the Kerr spacetime is given by [14]

$$ds^2 = -\left(1 - \frac{2M_1 r}{\Sigma}\right)dt^2 - \frac{4M_1 a r \sin^2\theta}{\Sigma}dt d\phi + \frac{\Sigma}{\Delta}dr^2 + \Sigma d\theta^2 + \left(r^2 + a^2 + \frac{2M_1 a^2 r \sin^2\theta}{\Sigma}\right)\sin^2\theta d\phi^2 \tag{2}$$

where $\Sigma \equiv r^2 + a^2\cos^2\theta$ and $\Delta \equiv r^2 - 2M_1 r + a^2$ with $a = \frac{J}{M_1}$ and J the angular momentum of the central BH. The metric in (2) is shown in Boyer-Lindquist coordinates. This metric reduces to the Schwarzschild metric in the limit $a \to 0$. The perturber is expected to be far away enough from M_1 so that the gravitational interactions can be considered to be weak. In this regime, where the radius of curvature of the external spacetime $\mathcal{R}$ is larger than the associated length scale of the central BH, $h_{\mu\nu}$ can be expanded into multipole moments. M_2 is ignored so M_1 and M_* can be considered as a binary. In that case, $\mathcal{R} \sim \sqrt{\frac{b^3}{M_{\text{tot}}}}$, where $M_{\text{tot}} = M_1 + M_*$ is the

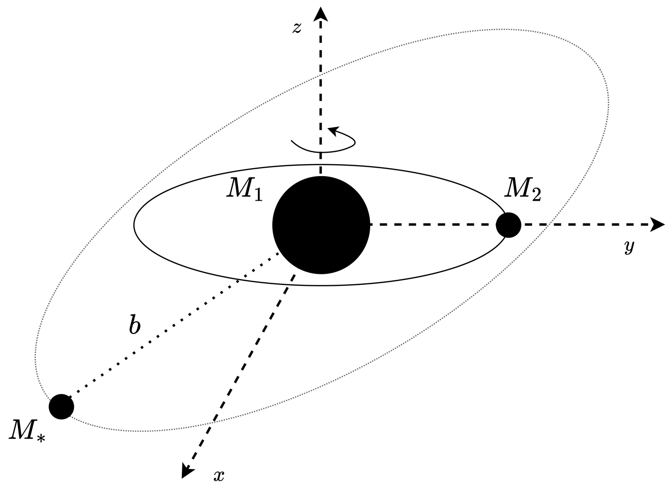

Figure 3: Schematic showing the EMRI with perturber. The central SMBH has mass M_1 and the stellar-mass object has mass M_2. The perturber has mass M_* and is positioned at a distance b from the large BH. The spin axis of the central BH coincides with the z-axis. The equatorial plane coincides with the (x, y)-plane.

total mass in the system [15]. The regime $M_1 \ll \mathcal{R}$ can be obtained in multiple ways. In this work, the weak-field approximation will be used. This approximation assumes $\frac{M_{\rm tot}}{b}$ to be small, while formally leaving no restrictions on the mass ratio $\frac{M_*}{M_1}$, although in this thesis, $M_* \sim M_2$ so that in practice this is also small. The weak-field approximation allows for a clean separation of scales, which allows one to consider the situation as a BH moving in an external post-Newtonian (PN) spacetime.

The metric perturbation has been determined using Kerr perturbation theory in previous research [8,16] by solving the Teukolsky equation. This method is computationally expensive, however. Calculating $h_{\mu\nu}$ using Schwarzschild perturbation theory is mathematically much less intense compared to Kerr perturbation theory, and still gives very accurate results [17]. In this work, $h_{\mu\nu}$ will be determined using Schwarzschild perturbation theory. $g_{\mu\nu}$ will be the Schwarzschild metric belonging to the central BH and the tidal moments in $h_{\mu\nu}$ will not contain spin effects. After the metric perturbation is calculated, M_1 will be treated as a Kerr BH again.

2.2.1 Tidal moments

The tidal environment (external spacetime) is described by the gravitoelectric tidal moments $\mathcal{E}_{ab}, \mathcal{E}_{abc}, \mathcal{E}_{abcd}, ...$, and the gravitomagnetic tidal moments $\mathcal{B}_{ab}, \mathcal{B}_{abc}, \mathcal{B}_{abcd}, ...$ The gravitoelectric tidal moments encode the dependence of the perturbation on the presence of M_*. The gravitomagnetic moments contain the information of the dynamics of the perturber. All moments are defined as 3-dimensional Cartesian tensors and scale with M_*, b and the orbital velocity of the perturber given by

$$u = \sqrt{\frac{M_{\rm tot}}{b}}. \tag{3}$$

The leading gravitoelectric and gravitomagnetic moments scale as

$$\mathcal{E}_{ab} \sim \frac{M_*}{b^3}, \mathcal{E}_{abc} \sim \frac{M_*}{b^4}, \mathcal{E}_{abcd} \sim \frac{M_*}{b^5}, \mathcal{B}_{ab} \sim \frac{M_* u}{b^3}, \mathcal{B}_{abc} \sim \frac{M_* u}{b^4}, \mathcal{B}_{abcd} \sim \frac{M_* u}{b^5}. \tag{4}$$

Time derivatives of the tidal moments add a factor $\frac{u}{b}$ to the scaling. These extra $\frac{1}{b}$ and $\frac{u}{b}$ factors act as extra suppression terms so only the quadrupole moments $\mathcal{E}_{ab}$ and $\mathcal{B}_{ab}$ are considered in this thesis. Having $M_1 \ll b$ implies that $u^2 \ll (1 + \frac{M_*}{M_1})$ and thus that

$$M_1 \Omega_{\phi,\rm td} \sim \left(1 + \frac{M_*}{M_1}\right)^{\frac{1}{2}} \left(\frac{M_1}{b}\right)^{\frac{3}{2}} \ll 1, \tag{5}$$

with $\Omega_{\phi,\rm td} \sim \frac{u}{b}$ being the orbital angular frequency of the perturber. This means that the timescale associated with variations in the tidal field is much longer than the one associated with the central BH, i.e., the perturber is slowly moving.

The tidal moments $\mathcal{E}_{ab}$ and $\mathcal{B}_{ab}$ are defined by the components of the Weyl tensor C_{abcd} belonging to the external spacetime as

$$\mathcal{E}_{ab} = (C_{0a0b})^{\rm STF}, \tag{6a}$$

$$\mathcal{B}_{ab} = \frac{1}{2}(\epsilon_{apq} C^{pq}{}_{b0})^{\rm STF}, \tag{6b}$$

where the STF sign indicates taking the symmetric, trace-free part and ϵ_{abc} is the Levi-Civita symbol in three dimensions with $\epsilon_{123} = 1$. From the transformation of the frame components of the Weyl tensor under a parity transformation, the parity of $\mathcal{E}_{ab}$ and $\mathcal{B}_{ab}$ can be deduced [18]. $\mathcal{E}_{ab}$ transforms as an ordinary Cartesian tensor and thus has even parity. $\mathcal{B}_{ab}$ transforms as a pseudotensor and thus has odd parity. From now on, $\mathcal{E}_{ab}$ and $\mathcal{B}_{ab}$ will be referred to as the even parity and odd parity moments, respectively.

The tidal moments appear in $\tilde{g}_{\mu\nu}$ in terms of irreducible tidal potentials $\mathcal{E}^{\rm q}$ and $\mathcal{B}^{\rm q}_A$. These tidal potentials each have a specific parity label and have multipole order $l = 2$. Spherical polar coordinates (t, r, θ, ϕ) will be used for the rest of the calculation of the perturbed metric $\tilde{g}_{\mu\nu}$. The even parity tidal potential is constructed as

$$\mathcal{E}^{\rm q}(t, \theta^A) = \sum_{-2 \le m \le 2} \mathcal{E}^{\rm q}_m(t) Y^{2m}(\theta^A), \tag{7}$$

where the sum over m ranges from $-l$ to l $(l = 2)$. The harmonic components $\mathcal{E}^{\rm q}_m$ are combinations of the components of $\mathcal{E}_{ab}$ [19]. The Y^{lm} are the scalar spherical harmonics depending only on the angles $\theta^A = (\theta, \phi)$. The scalar spherical harmonics satisfy the equation

$$\Omega^{AB} D_A D_B Y^{lm} = -l(l+1) Y^{lm}. \tag{8}$$

Here, $\Omega_{AB} = \mathrm{diag}[1, \sin^2\theta]$ is the metric of the unit two-sphere and D_A is the covariant derivative operator compatible with Ω_{AB}. The odd parity tidal vector potential is given by

$$\mathcal{B}^{\rm q}_A(t, \theta^A) = \frac{1}{2} \sum_{-2 \le m \le 2} \mathcal{B}^{\rm q}_m(t) X^{2m}_A(\theta^A), \tag{9}$$

where again the sum ranges from -2 to 2. The harmonic components $\mathcal{B}^{\mathrm{q}}_m$ are combinations of the components of $\mathcal{B}_{ab}$. The X^{lm}_A are the odd-parity vector harmonics given by

$$X^{lm}_A(\theta^A) = -\epsilon_A{}^B D_B Y^{lm}(\theta^A). \tag{10}$$

Here, ϵ_{AB} is the Levi-Civita tensor on the unit two-sphere with $\epsilon_{\theta\phi} = -\epsilon_{\phi\theta} = \sin\theta$ being the only nonzero components. The exact values of the spherical harmonics Y^{2m} and X^{2m}_A and the relations between $\mathcal{E}^{\mathrm{q}}_m, \mathcal{B}^{\mathrm{q}}_m$ and the components of their respective tidal moments are given in [20].

2.2.2 Calculating the perturbed metric

The tidally perturbed metric is expanded to order $(\frac{r}{b})^2\frac{M_*}{b}$ and $(\frac{r}{b})^2\frac{M_*}{b}u$ in the Regge-Wheeler gauge for the even and odd parity part, respectively. The Regge-Wheeler gauge confines the even parity components, which are included in $\tilde{g}_{\mu\nu}$ as $\mathcal{E}^{\mathrm{q}}$ multiplied by radial functions $e^{\mathrm{q}}_{\mu\nu}$, to the tt, rr and AB components of the metric. The odd parity components, which are included in $\tilde{g}_{\mu\nu}$ as $\mathcal{B}^{\mathrm{q}}_A$ multiplied by the radial functions b^{q}_μ, appear only in the tA and rA components of $\tilde{g}_{\mu\nu}$. The tidally deformed metric in the Regge-Wheeler gauge is given by

$$\tilde{g}_{tt} = -f + r^2 e^{\mathrm{q}}_{tt}\mathcal{E}^{\mathrm{q}}, \tag{11a}$$
$$\tilde{g}_{tr} = 0, \tag{11b}$$
$$\tilde{g}_{rr} = f^{-1} + r^2 e^{\mathrm{q}}_{rr}\mathcal{E}^{\mathrm{q}}, \tag{11c}$$
$$\tilde{g}_{tA} = r^3 b^{\mathrm{q}}_t \mathcal{B}^{\mathrm{q}}_A, \tag{11d}$$
$$\tilde{g}_{rA} = r^3 b^{\mathrm{q}}_r \mathcal{B}^{\mathrm{q}}_A, \tag{11e}$$
$$\tilde{g}_{AB} = r^2\Omega_{AB}(1 + r^2 e^{\mathrm{q}}\mathcal{E}^{\mathrm{q}}), \tag{11f}$$

where $f = 1 - \frac{2M_1}{r}$. The radial functions $e^{\mathrm{q}}_{tt}, e^{\mathrm{q}}_{rr}, e^{\mathrm{q}}, b^{\mathrm{q}}_t$ and b^{q}_r are obtained by solving the linearized vacuum Einstein equations. Their functional values are shown in table 1.

$e^{\mathrm{q}}_{tt} = -f^2$
$e^{\mathrm{q}}_{rr} = -1$
$e^{\mathrm{q}} = \frac{2M_1^2}{r^2} - 1$
$b^{\mathrm{q}}_t = \frac{2}{3}f$
$b^{\mathrm{q}}_r = 0$

Table 1: Expressions of the radial functions in equation (11).

The form of the tidal moments $\mathcal{E}^{\mathrm{q}}$ and $\mathcal{B}^{\mathrm{q}}_A$ are determined by matching the tidally deformed metric with a PN Schwarzschild metric. $\tilde{g}_{\mu\nu}$ holds in the region $r < r_{\max} \ll b$. The PN metric is valid at $r > r_{\min} \gg M_1$, so the values of the tidal moments can be obtained by this procedure in the range

$$M_1 \ll r_{\min} < r < r_{\max} \ll b. \tag{12}$$

Details on the metric matching procedure are shown in [20]. The resulting tidal moments are given by

$$\mathcal{E}_{ab} = -3\frac{M_*}{b^3} n_{\langle a} n_{b\rangle} + (1\mathrm{PN}), \tag{13a}$$

$$\mathcal{B}_{ab} = -6\frac{M_* u}{b^3}\epsilon_{pq(a} n_{b)} n^p \lambda^q + (1\mathrm{PN}). \tag{13b}$$

Where the angular brackets indicate taking the symmetric trace-free part of the vector product. The unit vectors are Cartesian and are expressed as

$$n_a = (\cos(\Omega_{\phi,\mathrm{td}} t), \sin(\Omega_{\phi,\mathrm{td}} t), 0), \tag{14a}$$
$$\lambda_a = (-\sin(\Omega_{\phi,\mathrm{td}} t), \cos(\Omega_{\phi,\mathrm{td}} t), 0). \tag{14b}$$

In this Cartesian frame, the z-axis is aligned with the angular momentum of M_1. The angular frequency of the tidal field is given by

$$\Omega_{\phi,\mathrm{td}} = \sqrt{\frac{M_{\mathrm{tot}}}{b^3}} + (1\mathrm{PN}), \tag{15}$$

which is the frequency of the perturber. The 1PN and higher order terms are ignored because they are of higher order in u and $\frac{M_*}{b}$ and thus are suppressed. Now that all components of the perturbed metric in (11) are obtained, the perturbation $h_{\mu\nu}$ can be found by subtracting the Schwarzschild metric from $\tilde{g}_{\mu\nu}$.

2.3 Kerr geodesics

Now that the metric perturbation induced by the tidal perturber has been obtained, the central BH can be treated as a Kerr BH again. The dynamics of the EMRI can be treated perturbatively due to its small mass ratio $\eta = \frac{M_2}{M_1}$. At leading order, we can approximate the secondary M_2 to be a test particle moving in the Kerr geometry of M_1. This motion is described by the geodesics of the spacetime and has three fundamental frequencies. These frequencies are important for studying tidal resonances. In this subsection, a short overview of the derivation of the fundamental frequencies will be shown, and a new set of variables will be introduced to simplify the classification of different orbits.

The orbit will be described using Boyer-Lindquist coordinates and parameterized by Mino time $\lambda = \int \frac{d\tau}{\Sigma}$, where $\Sigma = r^2 + a^2\cos^2\theta$. The advantage of using Mino time is that it decouples the r and θ velocity components and thus simplifies the geodesic equations describing the motion of the secondary. These geodesic equations are given by

$$\left(\frac{dr}{d\lambda}\right)^2 = R(r) = (E(r^2+a^2))^2 - \Delta(r^2 + (aE - L_z)^2 + Q), \tag{16a}$$
$$\left(\frac{d\cos\theta}{d\lambda}\right)^2 = \Theta(\cos\theta), \tag{16b}$$
$$\frac{dt}{d\lambda} = T_r(r) + T_\theta(\cos\theta) + aL_z, \tag{16c}$$
$$\frac{d\phi}{d\lambda} = \Phi_r(r) + \Phi_\theta(\cos\theta) - aE. \tag{16d}$$

The functions $\Theta(\cos\theta), T_r(r), T_\theta(\cos\theta), \Phi_r(r)$ and $\Phi_\theta(\cos\theta)$ are defined as

$$\Theta(\cos\theta) = Q - (Q + a^2(1-E^2) + L_z^2)\cos^2\theta + a^2(1-E^2)\cos^4\theta, \tag{17a}$$
$$T_r(r) = \frac{r^2+a^2}{\Delta} E(r^2+a^2), \quad T_\theta(\cos\theta) = -a^2E(1-\cos^2\theta), \tag{17b}$$
$$\Phi_r(r) = \frac{a}{\Delta} E(r^2+a^2), \quad \Phi_\theta(\cos\theta) = \frac{L_z}{1-\cos^2\theta}, \tag{17c}$$

with $\Delta = r^2 - 2M_1 r + a^2$ as before. The geodesics of Kerr spacetime have three constants of motion, the energy $E = -u_t$, the z-component of the angular momentum $L_z = u_\phi$ and the Carter constant $Q = u_\theta^2 + \cos^2\theta\left(a^2(1-E^2) + \left(\frac{L_z}{\sin\theta}\right)^2\right)$. Here, the u_μ are the covariant components of the four-velocity of the secondary. This project focuses on bound orbits, for which $r(\lambda)$ and $\cos\theta(\lambda)$ become periodic functions that are independent of each other. Expressions of their fundamental periods Λ_r and Λ_θ can be obtained using equation (16) and are given by

$$\Lambda_r = 2\int_{r_{\min}}^{r_{\max}} dr \left(\frac{dr}{d\lambda}\right)^{-1} = 2\int_{r_{\min}}^{r_{\max}} \frac{dr}{\sqrt{R(r)}}, \tag{18a}$$

$$\Lambda_\theta = 4\int_0^{\cos\theta_{\min}} d\cos\theta \left(\frac{d\cos\theta}{d\lambda}\right)^{-1} = 4\int_0^{\cos\theta_{\min}} \frac{d\cos\theta}{\sqrt{\Theta(\cos\theta)}}, \tag{18b}$$

where

$$r_{\min} = \frac{pM_1}{1+e}, \quad r_{\max} = \frac{pM_1}{1-e}, \quad I + (\mathrm{sgn}\ L_z)\theta_{\min} = \frac{\pi}{2}. \tag{19}$$

$r_{\min}$ and $r_{\max}$ are the radii of the periapsis and the apoapsis, respectively. The relations in equation (19) introduce new variables p, e, I that are very useful for characterizing orbits. Here, p is the semilatus rectum, e is the eccentricity and I is the inclination angle from the equatorial plane of M_1. The parameter $x = \cos I$ will often be used instead of the inclination angle. Together with the spin parameter a, these new parameters are very useful because they define an easy mapping of the entire parameter space for orbits. a and e are both bounded between 0 and 1, $-1 \geq x \geq 1$ and p is bounded from below by the separatrix. The separatrix is the point where the orbit of the secondary transitions from a bound orbit to a plunge orbit [21].

Equation (16) shows that both $\frac{dt}{d\lambda}$ and $\frac{d\phi}{d\lambda}$ are the sum of a function of r and a function of $\cos\theta$. These equations can be integrated to obtain

$$t(\lambda) = \Gamma\lambda + t^{(r)}(\lambda) + t^{(\theta)}(\lambda), \tag{20a}$$

$$\phi(\lambda) = \Gamma_\phi\lambda + \phi^{(r)}(\lambda) + \phi^{(\theta)}(\lambda). \tag{20b}$$

Here, Γ and Γ_ϕ are the t and ϕ frequencies with respect to Mino time respectively. A derivation of these Mino frequencies is found in [22]. The Mino frequencies of r and θ can be obtained from the periods and are given by

$$\Gamma_r = \frac{2\pi}{\Lambda_r}, \quad \Gamma_\theta = \frac{2\pi}{\Lambda_\theta}. \tag{21}$$

The Boyer-Lindquist frequencies $\omega_r, \omega_\theta, \omega_\phi$ can be obtained from the Mino frequencies as

$$\omega_{r,\theta,\phi} = \frac{\Gamma_{r,\theta,\phi}}{\Gamma}. \tag{22}$$

These frequencies have complicated expressions containing elliptic integrals so they are difficult to calculate by hand. Luckily, the Black Hole Perturbation Toolkit (BHPT) [23] contains fast functions of (a, p, e, x) to calculate these frequencies efficiently. More information on this Mathematica package can be found in section 3.

2.4 Jumps in constants of motion

This subsection will give a short overview of the derivation of the resonance condition and the equations used to calculate the jumps in the orbital constants $C \in \{E, L_z, Q\}$. The small mass ratio η allows the evolution of the orbit of the secondary to be described perturbatively. At leading order, the secondary will be treated as a massless test particle. Its dynamics at this order will thus be described by the Kerr geodesics belonging to the spacetime around M_1. These geodesics can be expressed as

$$\frac{dC}{d\tau} = 0. \tag{23}$$

Adding perturbations to these geodesics is difficult in this formulation. Action-angle variables are needed to easily describe these next-to-lowest-order terms. In the action-angle formalism, the equations of motion (the geodesics in this case) are written in terms of periodic variables q_i called angles that have corresponding actions J_i. The actions are given by the integrals of motion [24]

$$J_i = \frac{1}{2\pi}\oint u_i dq_i \tag{24}$$

and are functions of the orbital constants E, L_z and Q. The closed integral is performed over the period of the angle q_i. For the Kerr spacetime, the actions are given by [25]

$$J_t = -E, \quad J_r = \frac{1}{2\pi}\oint \frac{R(r)}{\Delta}dr, \tag{25a}$$

$$J_\phi = L_z, \quad J_\theta = \frac{1}{2\pi}\oint \Theta(\theta)d\theta, \tag{25b}$$

and are given in Boyer-Lindquist coordinates. The functions Δ, R and Θ are the same functions as given in section 2.3. The leading-order equations of motion in this action-angle formalism are given by

$$\frac{dq_i}{dt} = \omega_i, \tag{26a}$$

$$\frac{dJ_i}{dt} = 0, \tag{26b}$$

where the ω_i are the Boyer-Lindquist frequencies belonging to the orbit. These frequencies depend on the actions J_i. The actions, like E, L_z and Q, are conserved for geodesic motion. Perturbative effects can now be easily added to these equations of motion. In this section, only the next-to-lowest-order effects of the gravitational self-force and the tidal force are considered. The EMRI dynamics can then be expanded in the smallness parameters η and ϵ, where ϵ is expressed as

$$\epsilon = \frac{M_* M_1^2}{b^3}. \tag{27}$$

In this expansion, it is important to look at the relevant timescales of the dynamics. The three important timescales are the orbital timescale $\tau_{\mathrm{orb}} \sim M_1$, the radiation reaction timescale $\tau_{\mathrm{rad}} \sim M_1/\eta$ and the timescale of the perturber $\tau_{\mathrm{pert}} \sim \sqrt{\frac{b^3}{M_1}}$. The hierarchy of these timescales is

$$\tau_{\mathrm{rad}} \gg \tau_{\mathrm{pert}} \gg \tau_{\mathrm{orb}}. \tag{28}$$

This hierarchy allows for some simplification of the dynamics, which will be introduced later. With the self-force and tidal force added, the equations of motion are given by [26]

$$\frac{dq_i}{d\tau} = \tilde{\omega}_i(\mathbf{J}) + \eta g^{(1)}_{i,\mathrm{sf}}(q_r, q_\theta, \mathbf{J}) + \epsilon g^{(1)}_{i,\mathrm{td}}(q_r, q_\theta, q_\phi, (Q_\phi,)\mathbf{J}) + \mathcal{O}(\eta^2, \epsilon^2, \eta\epsilon), \tag{29a}$$

$$\frac{dJ_i}{d\tau} = \eta G^{(1)}_{i,\mathrm{sf}}(q_r, q_\theta, \mathbf{J}) + \epsilon G^{(1)}_{i,\mathrm{td}}(q_r, q_\theta, q_\phi, (Q_\phi,)\mathbf{J}) + \mathcal{O}(\eta^2, \epsilon^2, \eta\epsilon), \tag{29b}$$

where $\tilde{\omega}_i(\mathbf{J})$ are the frequencies w.r.t. proper time τ and Q_ϕ is the action-angle phase of the perturber. This phase is related to the perturber's frequency by

$$\Omega_{\phi,\mathrm{td}} = \frac{dQ_\phi}{dt}. \tag{30}$$

Q_ϕ noted between brackets in equation (29) because the tidal force terms do not depend on the perturber phase in the stationary case. The terms with subscript 'sf' are the self-force terms and thus scale with the mass ratio η. The terms with subscript 'td' are the tidal force terms and scale with the strength of the tidal field ϵ. Because of the axisymmetry of Kerr spacetime, the self-force terms do not depend on q_ϕ. This symmetry is broken when the perturber is introduced (unless it is positioned on the spin axis of M_1). The self-force consists of a conservative and a dissipative part. The conservative part is responsible for self-force resonances, which will be ignored completely. The dissipative part drives the inspiral and causes the conserved quantities to change with timescale τ_{rad}. This thesis focuses on the effects of the tidal force only so only the terms with subscript 'td' will be used. Because $\tau_{\mathrm{rad}} \gg \tau_{\mathrm{orb}}$, numerous orbits are completed before the radiation reaction changes the conserved quantities and frequencies significantly. This means that the average of the tidal force terms can be used instead of the terms themselves. This is the adiabatic approximation. The equations of motion in this approximation are[27]

$$\frac{dq_i}{d\tau} \approx \tilde{\omega}_i(\mathbf{J}), \tag{31a}$$

$$\frac{dJ_i}{d\tau} \approx \left\langle G^{(1)}_{i,\mathrm{td}}(q_r, q_\theta, q_\phi, (Q_\phi,)\mathbf{J}) \right\rangle, \tag{31b}$$

where the average is done over many orbits or the phase space spanned by the three angles. In the adiabatic approximation, the expansion in equation (29a) is truncated to lowest order in ϵ. This means that for the equations of motion for the q_i, the geodesic evolution is retrieved in the adiabatic approximation. For equation 29b, $G^{(1)}_{i,\mathrm{td}}$ can be expanded in a Fourier series

$$G^{(1)}_{i,\mathrm{td}}(q_r, q_\theta, q_\phi, (Q_\phi,)\mathbf{J}) = \sum_{n,k,m(,s)} G^{(1)}_{i,nkm(s)}(\mathbf{J}) e^{i(nq_r + kq_\theta + mq_\phi(+sQ_\phi))}, \tag{32}$$

where the s-part between brackets only appear in the dynamic case. The exponential in the angles generally oscillates in time, which means that most modes with nonzero $n, k, m(, s)$ vanish after the averaging over the angles. There are special cases where the exponential evolves slowly in time. This happens when the total angular phase $q_{nkm(s)} := nq_r + kq_\theta + mq_\phi(+sQ_\phi)$ is slowly changing with time. Meaning that the time derivative of this total angular phase vanishes in this case. This time derivative can be easily obtained using equation (31a) and is given by

$$\tilde{\omega}_{nkm(s)} := \frac{dq_{nkm(s)}}{d\tau} = n\tilde{\omega}_r + k\tilde{\omega}_\theta + m\tilde{\omega}_\phi(+s\tilde{\Omega}_{\phi,\mathrm{td}}) = 0. \tag{33}$$

This is the resonance condition. The last term includes the new perturber frequency $\tilde{\Omega}_{\phi,\mathrm{td}} = \frac{dQ_\phi}{d\tau}$, which is not the same as the original $\Omega_{\phi,\mathrm{td}}$ defined w.r.t. Boyer-Lindquist time. Note that it is possible to write the resonance condition with different parameterization. The resonance condition w.r.t. Boyer-Lindquist time is shown in equation (47). The parts containing s are again between brackets because they do not appear in the stationary resonance condition. A resonance occurs when there is a set of integers $(n, k, m(, s))$ that satisfies the resonance condition. The average of the tidal force will consist of contributions from the resonances with coefficients $G^{(1)}_{i,nkm(s)}$ and the trivial case $G^{(1)}_{i,000(0)}$. Since the tidal force is weak, the contribution of $G^{(1)}_{i,000(0)}$

is negligible compared to those of the $G^{(1)}_{i,nkm(s)}$, so that term will be ignored. This means that the change in the J_i is completely determined by tidal resonances. There are no limits on the integers n, k, m, s. In principle, the resonance condition is satisfied an infinite number of times (e.g., if for $n = 2, k = 0, m = 1$ it is satisfied, it will also be satisfied for $n = 4, k = 0, m = 2$ or $n = 200, k = 0, m = 100$ etc.). It is, however, expected that the resonances with high values of n, k, m, s are suppressed because they cover a large part of the 3-torus spanned by the angles q_i and thus average to lower contributions to the change in the actions. There are more restrictions on the resonance numbers (n, k, m, s), which will be discussed in section 4.

To determine if the perturber can be considered stationary or dynamic, it is important to look at the timescale of the resonance and compare it to other relevant timescales. The timescale of a tidal resonance is approximated as [16]

$$\tau_{\text{res}} \sim \sqrt{\frac{4\pi}{\Gamma}} \sim M_1\sqrt{\frac{1}{\eta}}, \tag{34}$$

where $\Gamma = n\dot{\hat{\omega}}_r + k\dot{\hat{\omega}}_\theta + m\dot{\hat{\omega}}_\phi$. The dots above the frequencies indicate a derivative with respect to τ, indicating the evolution rate of the frequencies due to the dissipative part of the self-force. This resonance timescale is smaller than τ_{rad}. Indicating that these changes in the J_i are quite "sudden" (still $\sim 10^2$ orbits), which is why these changes induced by tidal resonances are called 'jumps'. The perturber can be considered stationary if $\tau_{\text{res}} < \tau_{\text{pert}}$. This approximation generally holds in the weak field regime where the perturber is far away enough to be moving slowly. If the perturber gets close to M_1, the approximation may be violated and the perturber has to be treated as dynamic. Note that the perturber cannot come too close to the central BH. Otherwise, the weak field approximation will be violated, and the adiabatic approximation won't give accurate results. The dynamic case will have more resonances because of the extra integer s giving more freedom to the resonance condition. It will also have different jumps in the orbital constants compared to the stationary case due to the different form of the perturbation $h_{\mu\nu}$. However, since the perturber is moving at a fixed speed in the dynamic case, $\dot{\hat{\Omega}}_{\phi,\text{td}} = 0$ and thus τ_{res} is the same as in the static case.

Equation (31b) indicates the change in the actions due to the tidal force (which only has contributions from tidal resonances). The total change in the actions can be determined by integrating the rates of change

$$\Delta J_i \approx \epsilon \int_{-\infty}^{\infty} \left\langle G^{(1)}_{i,\text{td}}(q_r, q_\theta, q_\phi, (Q_\phi,)\mathbf{J})\right\rangle d\tau. \tag{35}$$

In the stationary case, this can be written in terms of Fourier modes as [28]

$$\Delta J_i \approx \epsilon \sum_{j=\pm 1} \sqrt{\frac{2\pi}{|j\Gamma|}} \exp\left[\text{sgn}(j\Gamma)\frac{i\pi}{4} + ij\chi_s\right] G^{(1)}_{i,jn,jk,jm}(\mathbf{J}), \tag{36}$$

In the dynamic case, the frequency domain equation for ΔJ_i is given by

$$\Delta J_i \approx \epsilon \sum_{j=\pm 1} \sqrt{\frac{2\pi}{|j\Gamma|}} \exp\left[\text{sgn}(j\Gamma)\frac{i\pi}{4} + ij\chi_d\right] G^{(1)}_{i,jn,jk,jm,js}(\mathbf{J}), \tag{37}$$

where the sum is only over $j = \pm 1$ to exclude resonances with (jn, jk, jm) where $|j| > 1$. These resonances occur at the same location as the resonance with integers (n, k, m), but lead to significantly smaller jumps. The square root represents the duration of the resonance, and the exponential represents the dependence of the jumps on the total phase χ_s, χ_d with which the EMRI enters the resonance. χ_s is defined as

$$\chi_s := nq_r + kq_\theta + mq_\phi\Big|_{\tau=\tau_{\rm res}}, \tag{38}$$

and $\chi_d := \chi_s + sQ_{\phi 0}$, where $Q_{\phi 0}$ is the phase the perturber enters the resonance with. The Fourier coefficients $G^{(1)}_{i,n,k,m}$ determine the amplitudes of the jumps. Equation (36) gives the jumps of the actions in the action-angle formalism. A transformation can be applied to equation (36) to get a similar equation for the jumps in the orbital constants C_i. From now on, the jumps in these C_i will be considered. The coefficients $G^{(1)}_{i,n,k,m}$ are now determined by the induced acceleration from the metric perturbation $h_{\mu\nu}$ in Kerr spacetime. The induced acceleration is given by[8]

$$a^\alpha = -\frac{1}{2}\left(g^{\alpha\beta} + u^\alpha u^\beta\right)\left(2\nabla_\rho h_{\beta\lambda} - \nabla_\beta h_{\lambda\rho}\right)u^\lambda u^\rho + \mathcal{O}(h^2), \tag{39}$$

where $u^\alpha = \frac{dx^\alpha}{d\tau}$ represents the velocity vector of the secondary, $g_{\mu\nu}$ is the background Kerr metric and $h_{\mu\nu}$ is the metric perturbation from section 2.2. The expansion is truncated at first order in $h_{\mu\nu}$ in the weak field limit. The induced acceleration can be related to the jumps in the C_i as

$$\frac{dE}{d\tau} = -a_t, \tag{40a}$$

$$\frac{dL_z}{d\tau} = a_\phi, \tag{40b}$$

$$\frac{dQ}{d\tau} = 2u_\theta a_\theta - 2a^2\cos^2\theta u_t a_t + 2\cot^2\theta u_\phi a_\phi, \tag{40c}$$

where a_μ are the covariant components of the acceleration. Note that in the stationary case, the jumps in E are zero due to time translation symmetry. This symmetry is broken when the perturber is treated as dynamic. For equatorial orbits, there is no velocity in the polar direction, so $u_\theta = 0, \cos^2\theta = 0, \cot^2\theta = 0$. Combining this with equation (40c), it can be seen that the jumps in Q are zero for equatorial orbits. The Fourier coefficients can be obtained from the rates in equation (40) using an inverse Fourier transform

$$\left\langle \frac{dC}{dt} \right\rangle\Big|_{nkm} = \frac{1}{\Gamma_t(2\pi)^3}\int_0^{2\pi} dq_r \int_0^{2\pi} dq_\theta \int_0^{2\pi} dq_\phi \frac{dC}{d\lambda} e^{-i(nq_r + kq_\theta + mq_\phi)}, \tag{41a}$$

$$\left\langle \frac{dC}{dt} \right\rangle\Big|_{nkms} = \frac{1}{\Gamma_t(2\pi)^4}\int_0^{2\pi} dq_r \int_0^{2\pi} dq_\theta \int_0^{2\pi} dq_\phi \int_0^{2\pi} dQ_\phi \frac{dC}{d\lambda} e^{-i(nq_r + kq_\theta + mq_\phi + sQ_\phi)}. \tag{41b}$$

In the stationary case, $C \in \{L_z, Q\}$, and in the dynamic case, $C \in \{E, L_z, Q\}$. Note that the induced acceleration is now parameterized with respect to Mino time λ. The angular brackets indicate averaging over the angles q_i and Q_ϕ, and the amplitudes in equation (41) are expressed in Boyer-Lindquist coordinates. The integrals over q_i require $\frac{dC}{d\lambda}$ to be written in terms of those angles as well, while the rates have been constructed in Boyer-Lindquist coordinates through a^α and u^α. This problem can be avoided by transforming equation (41) to a Mino time parameterization. This is done by introducing new Mino times $\lambda_i = \frac{2\pi}{\Lambda_i}q_i$ with $i \in \{r, \theta, \phi\}$, where Λ_i are the Mino time periods ($\Lambda_\phi = \frac{2\pi}{\Gamma_\phi}$, and Λ_r and Λ_θ are defined in equation (18)). The Boyer-Lindquist coordinates are then reparameterized using λ_i. Expressions of these coordinates as function of these new Mino times can be found in[22].

The jump amplitudes can be calculated for a specified location in the (a, p, e, x) parameter space. The aim is to calculate the coefficients at the point of a certain resonance (classified by $\{n, k, m(, s)\}$), so p can be fixed for a certain combination of (a, e, x) by solving the resonance condition with the relevant integers. That leaves the subspace spanned by a, e and x, which specifies the orbit that will be considered. At the specified point in this subspace, the stationary case average of the rates can be determined by

$$\left\langle \frac{dC}{dt} \right\rangle\Bigg|_{nkm}(a,e,x) = \frac{1}{\Gamma_t \Lambda_r \Lambda_\theta \Lambda_\phi} \int_0^{\Lambda_r} d\lambda_r \int_0^{\Lambda_\theta} d\lambda_\theta \int_0^{\Lambda_\phi} d\lambda_\phi \frac{dC}{d\lambda}\bigg|_{nkm}(a,e,x) e^{-i\left(n\frac{2\pi}{\Lambda_r}\lambda_r + k\frac{2\pi}{\Lambda_\theta}\lambda_\theta + m\frac{2\pi}{\Lambda_\phi}\lambda_\phi\right)}, \tag{42}$$

for a specific combination of n, k and m. In the dynamic case this becomes

$$\left\langle \frac{dC}{dt} \right\rangle\Bigg|_{nkms}(a,e,x) = \frac{1}{2\pi\Gamma_t \Lambda_r \Lambda_\theta \Lambda_\phi} \int_0^{\Lambda_r} d\lambda_r \int_0^{\Lambda_\theta} d\lambda_\theta \int_0^{\Lambda_\phi} d\lambda_\phi \int_0^{2\pi} dQ_\phi \frac{dC}{d\lambda}\bigg|_{nkms}(a,e,x) e^{-i\left(n\frac{2\pi}{\Lambda_r}\lambda_r + k\frac{2\pi}{\Lambda_\theta}\lambda_\theta + m\frac{2\pi}{\Lambda_\phi}\lambda_\phi + sQ_\phi\right)}. \tag{43}$$

The rates $\frac{dC}{d\lambda}\big|_{nkm(s)}$ are now dependent on (a, e, x) through the new parameterization of the coordinates. The functional form of these rates differs significantly between the stationary and the dynamic case due to the difference in $h_{\mu\nu}$ between the cases. Note that the e with the exponent does not indicate the eccentricity. The quantities calculated using equations (42) and (43) can be used in equations (36) and (37) to obtain the jumps ΔC.

2.4.1 The two-for-one deal

An analytical relation between the rates of L_z and Q was derived[29] called the two-for-one deal. This equation relates the rate in Q to the rate in L_z as

$$\frac{dQ}{d\tau} = \frac{\frac{\pi a k}{m}\sqrt{1-E^2}\,y_+ - 2L_z\left(K\left[\left(\frac{y_-}{y_+}\right)^2\right] - \Pi\left[y_-^2, \left(\frac{y_-}{y_+}\right)^2\right]\right)}{K\left[\left(\frac{y_-}{y_+}\right)^2\right]} \frac{dL_z}{d\tau}, \tag{44}$$

where K and Π respectively are the complete elliptic integrals of the first and third kind, and $y_\pm^2$ are given by

$$y_\pm^2 = \frac{a^2(1-E^2) + L_z^2 + Q \pm \sqrt{(a^2(1-E^2) + L_z^2 + Q)^2 + 4a^2(E^2-1)Q}}{2a^2(1-E^2)}. \tag{45}$$

This relation holds for a stationary perturber with $m \neq 0$. When $m = 0$, azimuthal symmetry forces the jumps in L_z to be zero for all orbits. The two-for-one deal can be derived the other way around (see Appendix A) to obtain the rate in L_z from the rate in Q. The relation is as follows

$$\frac{dL_z}{d\tau} = \frac{K\left[\left(\frac{y_-}{y_+}\right)^2\right]}{\frac{\pi a k}{m}\sqrt{1-E^2}\,y_+ - 2L_z\left(K\left[\left(\frac{y_-}{y_+}\right)^2\right] - \Pi\left[y_-^2, \left(\frac{y_-}{y_+}\right)^2\right]\right)} \frac{dQ}{d\tau}. \tag{46}$$

The new prefactor is the inverse of the prefactor from equation (44). This flipped two-for-one deal still only holds in the stationary configuration, but now for $k \neq 0$ and $m \neq 0$. Equation

(46) puts restrictions on the rate of L_z for equatorial orbits. Since $\frac{dQ}{d\tau} = 0$ for orbits in the equatorial plane, $\frac{dL_z}{d\tau} = 0$ at $x = \pm 1$ when $k \neq 0, m \neq 0$ (the rate in L_z is also zero for $m = 0$ of course). This means that resonances with $k = 0, m \neq 0$ are the only tidal resonances that can cause dephasing in the waveform for equatorial orbits. These resonances will only give nonzero jumps in L_z for these orbits.

3 The code

Calculating the jump amplitudes analytically is not realistic. The functional form of the Boyer-Lindquist frequencies in the resonance condition, and the reparameterized Boyer-Lindquist coordinates in the rates $\frac{dC}{d\lambda}\Big|_{nkm(s)}$ in equations (42) and (43)involve elliptic integrals that cannot be done by hand. This means that numerical methods have to be used. A Mathematica code was developed to perform the calculations of the jump amplitudes $\left\langle\frac{dC}{dt}\right\rangle\Big|_{nkm(s)}$. This code can perform, when possible, subcalculations analytically, and perform the calculations that are too complicated numerically. Figure 4 shows the most important calculation steps in a flowchart. This section will explain the most important parts of this code. Results gathered using this code are shown in sections 4 and 5.

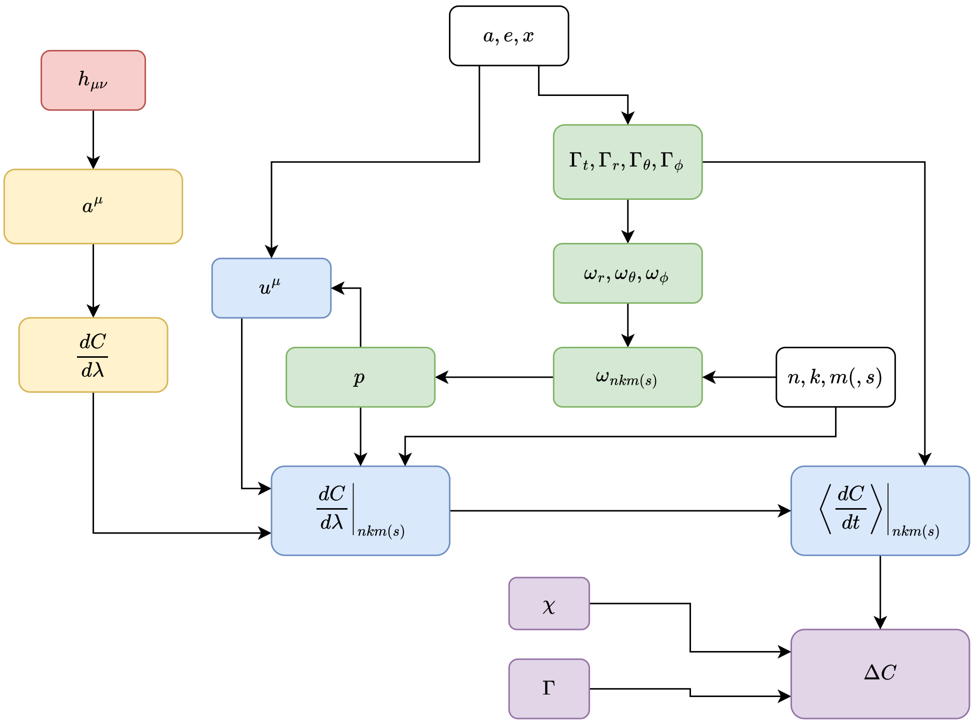

Figure 4: Flowchart showing the calculation of the jump sizes ΔC. Note that not all relevant quantities are shown for clarity. The quantities in white are input parameters for every calculation. The quantities in yellow represent the calculation of the rates in the orbital constants, and are discussed in section 3.1. The green quantities indicate the calculation of the location in the (a, p, e, x) parameter space. This calculation is discussed in section 3.2. The blue quantities represent performing the averaging procedure, and are discussed in section 3.3. The calculation of $h_{\mu\nu}$ has been discussed in section 2.2. The part in purple can be performed in waveform modeling codes that can model tidal resonances like the FastEMRIWavefroms (FEW) Python package[13].

3.1 Induced acceleration and rates

This subsection will focus on the yellow part of figure 4, which covers the (pretty straightforward) analytical calculation of the rates $\frac{dC}{d\lambda}$. The metric perturbation $h_{\mu\nu}$ is used in equation (39) to obtain the induced acceleration a^{μ}. In the code, this was done using the GeneralRelativityTensors package[23]. To specify the components of the four velocity u^{μ}, the location in the orbital parameter space is needed. For this reason, the components of u^{μ} are not specified in the calculation. The rates are calculated from the acceleration using equation (40). The parameterization is completely dependent on the parameterization of the components of u^{μ} and x^{μ}. The aim is to obtain the rates in terms of Mino time, so x^{μ} and u^{μ} have to be functions of λ.

The rates contain many trigonometric functions of the variables θ, ϕ, Q_{ϕ}. These functions can be rewritten in terms of exponential functions. This procedure makes the simplifying of the rates easier for Mathematica. These rates are now ready for implementation in the part of the code that calculates the jump amplitudes.

3.2 The resonance condition

This subsection covers the methods used to solve the resonance condition. This is done to obtain the location in the (a, p, e, x) parameter space. The resonance condition that will be solved is given by

$$\omega_{nkm(s)} := \frac{dq_{nkm(s)}}{dt} = n\omega_r + k\omega_\theta + m\omega_\phi(+s\Omega_{\phi,\mathrm{td}}) = 0. \tag{47}$$

All frequencies in equation (47) are Boyer-Lindquist frequencies. The frequencies are implemented in this equation using the KerrGeoFrequencies function from the KerrGeodesics package[23]. This function gives the value of the Boyer-Lindquist frequencies for a given combination of a, p, e and x. As mentioned earlier, the functional dependence of these frequencies is very complicated. Meaning that the resonance condition can only be solved using numerical solving methods.

The Mathematica function FindRoot is used to find solutions to the resonance condition. This function uses the Newton-Raphson method to find a solution to a specified equation when given an initial guess p_0. A description of this method can be found in[30]. Due to the Newton-Raphson method being only locally convergent, FindRoot is less robust than other functions like NSolve. FindRoot is still used in this project because it is also much faster, and there are some precautions that can be taken to make this function more reliable.

As a start, FindRoot allows a search domain to be specified. Making it only look for solutions in a certain range of p values. It is known that p has to be bounded from below by the separatrix p_s, so this value can be used to be the lower bound of the search domain. A method to calculate p_s for a given (a, e, x) was developed[21] and implemented in the KerrGeoSeparatrix function[23]. There is no absolute upper bound on p, so this bound has to be chosen. Most EMRIs enter the LISA observational band in the last stage of their inspiral. This means that high values of p belong to orbits before entering the LISA band. The exact p value when an EMRI enters the observational band is dependent on (a, e, x), the masses of the bodies and their distance from us. A conservative guess of $p = 100 + p_s$ was used as the upper bound for FindRoot.

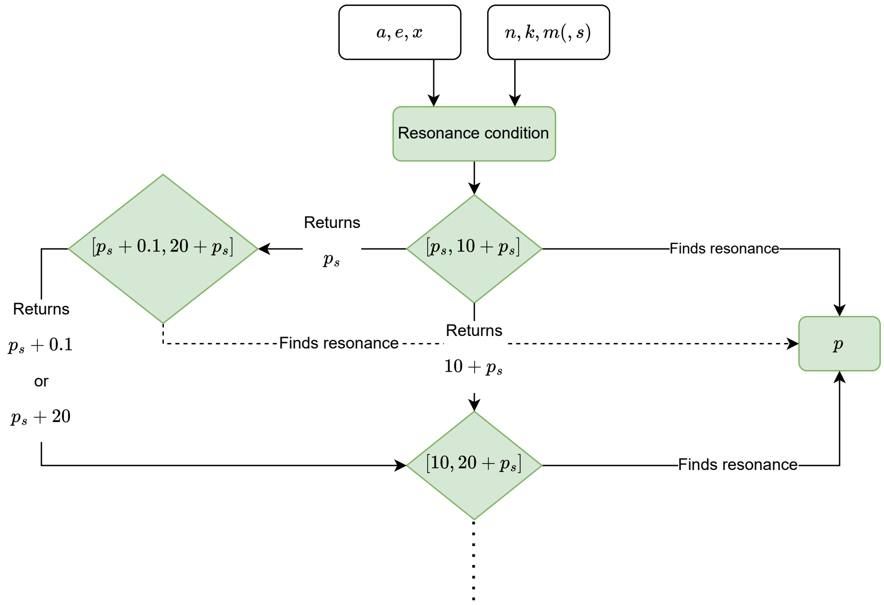

Figure 5: Flowchart showing the root finding procedure. The diamond cells containing the ranges of p values indicate the steps where FindRoot is used to find a solution to the resonance condition in the specified range. The white cells indicate the input variables for the root finder. The dotted line at the bottom indicates the possible continuation of the procedure to higher p subdomains. The root finding procedure stops when a resonance has been found.

The range to find p is still very large. The locally convergent nature of FindRoot causes the function to be less trustworthy for larger search domains. This can be avoided by splitting up the search domain into multiple smaller domains. An overview of the root finding procedure is shown in figure 5. The search starts with the lowest values in the domain $p \in [p_s, 10 + p_s]$ with an initial guess of $p_0 = p_s + 2$. If FindRoot indicates that it expects the solution to be larger than the upper bound of the current subdomain, the search is continued in the next domain. In the case that FindRoot expects the solution to be lower than p_s, the search is restarted with a higher initial guess p_0 and upper bound, and a slightly higher lower bound. This is to ensure that FindRoot didn't miss the solution in the first range because it got misled by a too low value of p_0. The division of the root finding procedure into multiple steps increases the accuracy, but also slows the procedure down. This procedure is still much faster than using NSolve, however (the root finder usually takes less than ten seconds compared to NSolve taking more than a minute).

Even with the measures that have been mentioned, the root finder is still not robust. Especially near the separatrix p_s, where the frequencies $\omega_r, \omega_\theta, \omega_\phi$ start to diverge. With the aim to create a more stable resonance finder, a new way of constructing the resonance condition was developed. This new resonance condition is constructed using the simple relation between the Boyer-Lindquist frequencies and their respective Mino frequencies in Eq. (22). The new resonance condition is now parameterized using Mino time and is given by

$$\Gamma\omega_{nkm(s)} = n\Gamma_r + m\Gamma_\theta + m\Gamma_\phi(+s\Omega_{\phi,\mathrm{td}}\Gamma) = 0. \tag{48}$$

The functional form of the Mino frequencies in terms of (a, p, e, x) is constructed using formulas in[31] and[22]. It appears that the expressions of the Mino frequencies is simpler than those belonging to the Boyer-Lindquist frequencies. This difference can be noticed because the use of this new resonance condition as the input for FindRoot increases the speed of the resonance finder. The use of the new resonance condition makes the resonance finder more robust than before for some $(n, k, m(, s))$, and less robust for others. Again, this loss of robustness seems to happen near the separatrix. The resonance finder can be made overall more trustworthy by making it solve both resonance conditions in the domain $p \in [p_s, 10 + p_s]$. If FindRoot finds a solution with one of the resonance conditions, that solution likely belongs to a resonance. As an extra test, the solution can be filled back into the resonance condition to see if the result is (virtually) zero. If FindRoot can't find a solution to both resonance conditions, it is probably safe to assume that there are no solutions in that domain. Note that, due to and error made, this solving of both resonance contours is not done in this project. Only Eq. (33) is solved in the domain $p \in [p_s, 10 + p_s]$. For higher p domains, it suffices to only find a solution to one resonance condition. For this part of the resonance finder, Eq. (48) is used as the resonance condition because it is faster.

3.3 Calculating the jump amplitudes

This subsection discusses the blue part of figure 4, which belongs to the calculation of the averaging integrals to obtain the $\left\langle \frac{dC}{dt} \right\rangle\Big|_{nkm(s)}$. Now that the location of the resonance and the dependence of the rates on x^μ and u^μ are known, they can be combined to obtain the expression of the rates as function of (a, p, e, x) and the Mino times. The (a, p, e, x) belonging to the resonance can be used as input for the KerrGeoOrbit function in Mathematica[23]. This function gives the Boyer-Lindquist coordinates (t, r, θ, ϕ) as function of Mino time λ, and the Mino frequencies $(\Gamma, \Gamma_r, \Gamma_\theta, \Gamma_\phi)$. These objects can then be used to calculate the Mino periods $(\Lambda_t, \Lambda_r, \Lambda_\theta, \Lambda_\phi)$. Three different Mino times are then introduced to parameterize the Boyer-Lindquist coordinates as $(r(\lambda_r), \theta(\lambda_\theta), \phi(\lambda_r, \lambda_\theta, \lambda_\phi))$. The coordinate t is not used, so it can be ignored.

In the next step, the rates are imported and the position of the perturber is specified by filling in the angles θ_y and θ_z. Then, the components of x^μ and u^μ can be filled into the rates. Before the components that are dependent on Mino time are filled in, it is important to note that the integrals over Q_ϕ and λ_ϕ can be done analytically. Details on the insertion of their solutions can be found in[17]. A grid iterating over $\lambda_r, \lambda_\theta$ is constructed. The size of the grid is determined by the parameter n_s. Higher values of n_s increase the accuracy of the averaging integral, and thus the accuracy of the estimates of the jump amplitudes. However, the computation time of the jump amplitudes scales with n_s^2, so a balance between accuracy and speed has to be determined. For this project, n_s was kept at 61. The components of x^μ, u^μ are inserted at every point on the grid. The grid points are then interpolated. Finally, NIntegrate is used to numerically integrate over the function obtained from the interpolation procedure. The results of these numerical integrals are the jump amplitudes $\left\langle \frac{dC}{dt} \right\rangle\Big|_{nkm(s)}$.

The aim is to obtain the jumps in the orbital constants for every configuration of the system, for each resonance. At a given combination of $n, k, m(, s)$, the parameter space consists of the variables $a, e, x, \theta_y, \theta_z(, \Omega_{\phi,\mathrm{td}}), M_1, M_2, M_*, b$ for the jump amplitudes. The dephasing of the waveform for different values of $\theta_y, M_1, M_2, M_*, b$ can be obtained from the scaling relation [16]

$$\Delta\Psi_i' = \Delta\Psi_i \left(\frac{M_1'}{M_1}\right)^{\frac{7}{2}} \left(\frac{M_2'}{M_2}\right)^{-\frac{3}{2}} \left(\frac{M_*'}{M_*}\right) \left(\frac{b'}{b}\right)^{-3} \left(\frac{f_m(\theta_y')}{f_m(\theta_y)}\right), \tag{49}$$

where $\Delta\Psi_i$ is the accumulated phase and $f_m(\theta_y)$ incorporates the dependence of the accumulated phase on the inclination of the perturber θ_y. Details on $f_m(\theta_y)$ (including a derivation) can be found in [17]. Equation (49) indicates that $\theta_y, M_1, M_2, M_*, b$ do not need to be varied over in the code. When calculating the jumps, it is important to fix these variables in a way that makes the scaling relation remain valid (e.g., choose θ_y for which $f_m(\theta_y) \neq 0$). The dependence of the jumps on θ_z is also trivial, so it also doesn't need to be varied. It was expected that the dependence of the jump amplitudes on $\Omega_{\phi,\mathrm{td}}$ was trivial as well, so the calculations were done for one value of $\Omega_{\phi,\mathrm{td}}$. Later, it was discovered that the dependence of the jumps can be nontrivial (see section 4.2). Because the addition of $\Omega_{\phi,\mathrm{td}}$ adds an extra dimension to the parameter space that needs to be iterated over, accurate data on the jumps were not obtained.

For the stationary case, only a, e, x are left. Because prograde orbits and retrograde orbits give different combinations of n, k, m, the parameter space is split into prograde and retrograde orbits ($x > 0, x < 0$, respectively). In the two parts of the parameter space, a grid was created. In this grid, $a \in [0.1, 0.5, 0.9]$ and $e \in [0.10, 0.15, \cdots, 0.80, 0.85]$ in both parts of the (a, e, x) space. For prograde orbits, $I \in [1°, 5°, 10°, \cdots, 80°, 85°, 89°]$, and for retrograde orbits, $I \in [91°, 95°, 100°, \cdots, 170°, 175°, 179°]$ where $x = \cos(I)$. The equatorial plane corresponds to $I = 0°$ for prograde orbits and corresponds to $I = 180°$ for retrograde orbits. The set of resonances is also split into prograde and retrograde. For each prograde resonance, the jump amplitudes are calculated for every point on the prograde grid. For each retrograde resonance, the jump amplitudes are calculated on the retrograde grid.

4 Resonance contours

4.1 Stationary case resonance contours

For the stationary case, all resonances with $-4 \leq n \leq 4$, $-4 \leq k \leq 4$ and $-2 \leq m \leq 2$ are considered. It is expected that resonances with higher (n, k, m) lead to significantly smaller jumps in the orbital constants. Because only quadrupolar $l = 2$ moments of the tidal perturbation are considered in this thesis, m is only allowed to range between -2 and 2. These initial restrictions on n, k and m leave 405 possible combinations of (n, k, m). Most of these combinations do not give a relevant resonance, so these numbers are filtered out as much as possible using the following set of selection rules.

- It has been shown that the tidally induced jumps in L_z and Q are invariant under reflections of the orbit in the equatorial plane[17]. This means that the jumps in L_z and Q are zero unless $k + m =$ even, so only resonances with $k + m =$ even will be considered.
- If there exists a set of resonance numbers (n, k, m), there is a resonance with numbers (jn, jk, jm) at the exact same location for any integer j with $|j| > 1$. It is expected that these resonances with (jn, jk, jm) are less important since they have higher numbers, so they will be ignored.
- Since (n, k, m) and ($-n$, $-k$, $-m$) represent the same resonance, we will avoid unnecessary computations by only considering resonances where the first nonzero number is positive.
- For prograde orbits, all orbital frequencies ω_r, ω_θ, ω_ϕ are positive. Thus, only sets of numbers with $k < 0$ and/or $m < 0$ can lead to a resonance, so only (n, k, m) with $k < 0$ and/or $m < 0$ are considered for prograde orbits.
- For retrograde orbits, ω_r and ω_θ are positive and ω_ϕ is negative. Only sets of numbers with $k < 0$ and/or $m > 0$ (note the change for m compared to the prograde situation) can thus lead to a resonance, so only (n, k, m) with $k < 0$ and/or $m > 0$ are considered for retrograde orbits.

The application of the selection rules leaves 110 potential resonances. For these (n, k, m) combinations, a rough test is performed where the resonance finder is used to find a resonance on a grid that roughly spans the parameter space. If the resonance finder can't find a resonant p value below 100, the set of numbers is considered not relevant because the resonance happens outside the LISA band. The resonance contours of the remaining 24 sets of resonance numbers are calculated using the resonance finder. Here, the parameter space is divided into prograde ($x > 0$) and retrograde ($x < 0$) orbits.

4.1.1 Prograde orbits

The prograde resonance contours for a =0.5 and $I = 50°$ are shown in figure 6. The black and red contours represent even and odd m resonances, respectively. In all plots in this section, a and p are normalized to M_1. The first thing that can be noticed from figure 6 is that almost all resonance contours have a similar dependence on e. The dependence of the $n = 1$ resonances on e looks a bit different compared to the rest in figure 6 because they basically follow the separatrix. It can also be seen that there are no $n = 2$ resonances. This can be explained by looking at the orbital frequencies. Almost throughout the parameter space, ω_θ and ω_ϕ are significantly closer to each other than to ω_r. For prograde, ω_r is also lower than the other frequencies. Considering this, the resonance numbers can be analyzed to good accuracy by only looking at the values of

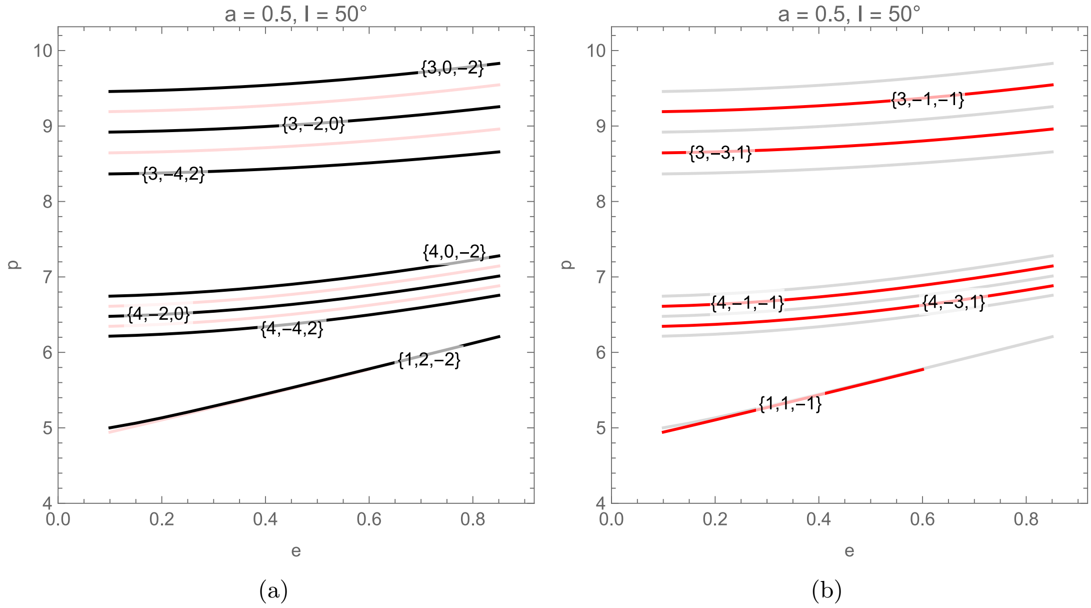

Figure 6: Prograde resonance contours showing the resonant p value as function of e for fixed a and I. The contour labels correspond to numbers $\{n,\ k,\ m\}$. The resonances with even m are black and labeled in (a) and the resonances with odd m are red and labeled in (b).

n and $k+m$. In this simplification, the sets of numbers with $n = 2$ can be divided into four groups: numbers with $k+m = -6,\ -4,\ -2$ or 0. Since ω_θ and ω_ϕ are much larger than ω_r at low p, there can only be a resonance at low p if

$$|n| > |k+m|, \tag{50}$$

which means that, for $n = 2$, $(n,\ k,\ m)$ with $k+m = -6,\ -4$ and -2 can't lead to a resonance at a low p. Looking at figure 7, it may be possible that the $k+m = -2$ sets have resonances at high p, but these will be outside the LISA band and thus not relevant.

Figure 7 shows the dependence of the orbital frequencies on p for high and low a. It can be seen that the difference between ω_θ and ω_ϕ is larger for high a and goes down with increasing p. The frequencies increase with decreasing p, except for ω_r when it approaches the separatrix, it shows sudden a steep drop. Because ω_r is always smaller than the other two frequencies, resonance number sets with $|n| < |k+m|$ cannot have a resonance. For $n = 1$, that means that only resonances with $k+m = 0$ can have a resonance. These $n = 1$ resonances appear mostly near the separatrix because there, the difference between ω_θ and ω_ϕ can become equal to ω_r. There are other resonances with $k+m = 0$ like $(3,\ 2,\ -2)$. These resonances lie even closer to the separatrix than the $n = 1$ resonances. These resonances with $n > 1$ and $k+m = 0$ will be less impactful than the $n = 1$ resonances and will thus be ignored.

The functional dependence of the weighted sum of the frequencies ω_{nkm} on p is shown in figure 8 for the $(3,\ -4,\ 2)$ and the $(3,\ 0,\ -2)$ resonances. It can be seen that the ω_{nkm} of these two resonances have a similar dependence on p. This shape of the ω_{nkm} seems to occur for all

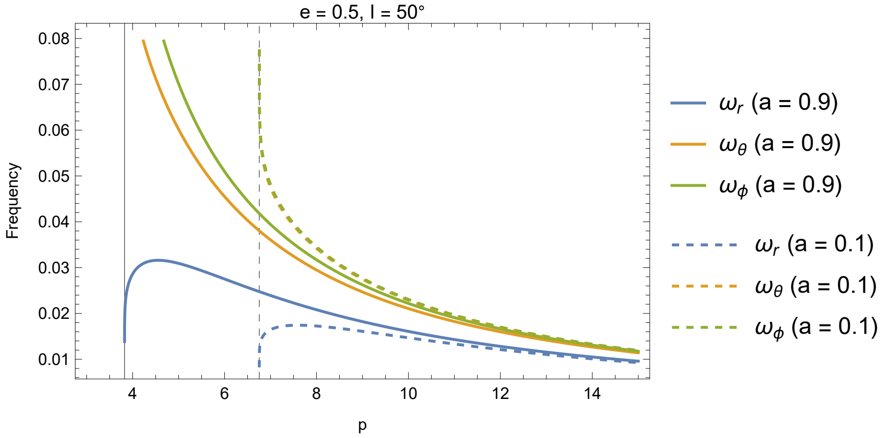

Figure 7: Prograde frequency plots showing the value of the frequencies as function of p for multiple values of a. The solid lines represent the frequencies at $a = 0.9$ and the dashed lines represent the frequencies at $a = 0.1$. The solid and dashed vertical lines show the location of the separatrix at $a = 0.9$ and $a = 0.1$, respectively.

resonances with $n \leq 4$. One important feature to note is that the dependence of ω_{nkm} on p is not injective. The curves increase very fast from negative values to positive values at low p. Then, the curves slowly decrease with increasing p. For large p, the weighted sum of the frequencies converge to

$$\varphi_s = (n + k + m)\omega_{\text{kep}}, \tag{51}$$

where ω_{kep} is the Keplerian frequency $\sqrt{\frac{M_1+M_2}{p^3}}$, so it is expected that there is no more than one solution to the stationary resonance condition in the LISA band. Note that in the dynamic case, it is possible to get more than one resonance belonging to one set of $(n,\, k,\, m,\, s)$. $\Omega_{\phi,td}$ is just a parameter as it only depends on M_1, M_* and b, which means that it only shifts the ω_{nkms} curve up or down, so that there are resonances where the ω_{nkms} shoots up from negative to positive value at low p, and then converges again to a negative value at high p. It is expected that there will be no more than two resonances for one $(n,\, k,\, m,\, s)$ in the dynamic case.

For $n = 3$ and $n = 4$, looking at resonances where $0 < k + m < n$ leaves only resonances where $k + m = -2$. The contours of these resonances are shown in figure 6. Here, the relatively small difference between ω_θ and ω_ϕ result in the clustering of resonances with the same n. Because ω_ϕ is larger than ω_θ, ω_{n0-2} has larger values than ω_{n-42}. Looking at the general shape of an ω_{nkm} (see figure 8), it can be deduced that lower values of ω_{nkm} gives a higher resonant p. This matches with the order of the contours in figure 6. The relative position of the $n = 3$ and $n = 4$ bands can be explained similarly. The extra ω_r for $n = 4$ resonances compared to $n = 3$ resonances results in larger values for ω_{nkm} and thus lower p values for the resonance contours.

The prograde resonance contours for different a are shown in figure 9. Figure 9a shows the resonance contours for small a, which group together even more than those for $a = 0.5$ in figure 6. This is to be expected because the difference between the two angular frequencies decreases as a goes to zero. At $a = 0$, ω_θ and ω_ϕ are the same. Consequently, in that limit, all resonances with the same $n, k + m$ overlap. It can also be seen that the $n = 1$ resonances are not fully complete in figure 9a. These resonance contours seem to dive under the separatrix around $e = 0.5$. It

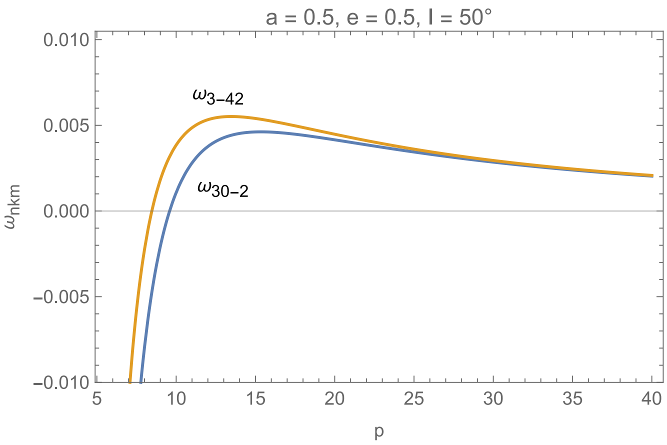

Figure 8: Functional dependence of ω_{3-42} (orange line) and ω_{30-2} (blue line) on p at $a = 0.5$, $e = 0.5$ and $I = 50°$.

is difficult to determine the exact location of this crossing because the resonance finder suffers from precision loss around the separatrix. The same reason explains why the (1, 1, -1) resonance contour seems to start at $e = 0.2$. It is expected that this resonance contour should extend to lower e, but the resonance finder did not find a resonance in that part of the parameter space. Figure 6, showing the resonance contours at $a = 0.5$, indicates that there seems to be a crossing of the separatrix around $e = 0.6$ for the (1, 1, -1) resonance, but no crossing for the (1, 2, -2) resonance. Again, note that the exact location of this crossing is unknown due to behavior of the resonance finder close to the separatrix.

The resonance contours at $a = 0.9$ for prograde orbits are shown in figure 9b. They are consistent with the resonances modeled in previous work [16]. There are no bands anymore because the difference between the polar and azimuthal frequencies has become too large. In fact, the resonance contours start to intersect at low p. This will complicate the waveform modeling process because the FEW package has trouble handling resonances that intersect or are very close to each other. The $a = 0.1$ resonances in figure 9a could also be difficult to model for the latter reason. These issues need to be addressed in order to model the entire evolution of the waveform accurately. Another notable observation that can be made from figure 9b is that the $n = 1$ resonance contours are not (almost) on top of each other anymore. The (1,2,-2) resonance contour even seems to occur for larger p values than some of the $n = 4$ resonances. This shows that these $n = 1$ resonances can become important at high a. It is expected, however, that the other $k + m = 0$ resonances are still too close to the separatrix to become important.

Figure 9 also shows another general trend in the resonance contours. As a increases, all resonances seem to happen at a lower p. This happens because, when a increases, ω_r increases and ω_θ and ω_ϕ decrease. Resulting in an overall upward shift of ω_{nkm} and thus a lower resonant p value. ω_θ decreases faster than ω_ϕ, so the resonance contours with a higher value of k drop more. Note that the separatrix also drops when a increases, which is why the resonances can happen at such low p for high a.

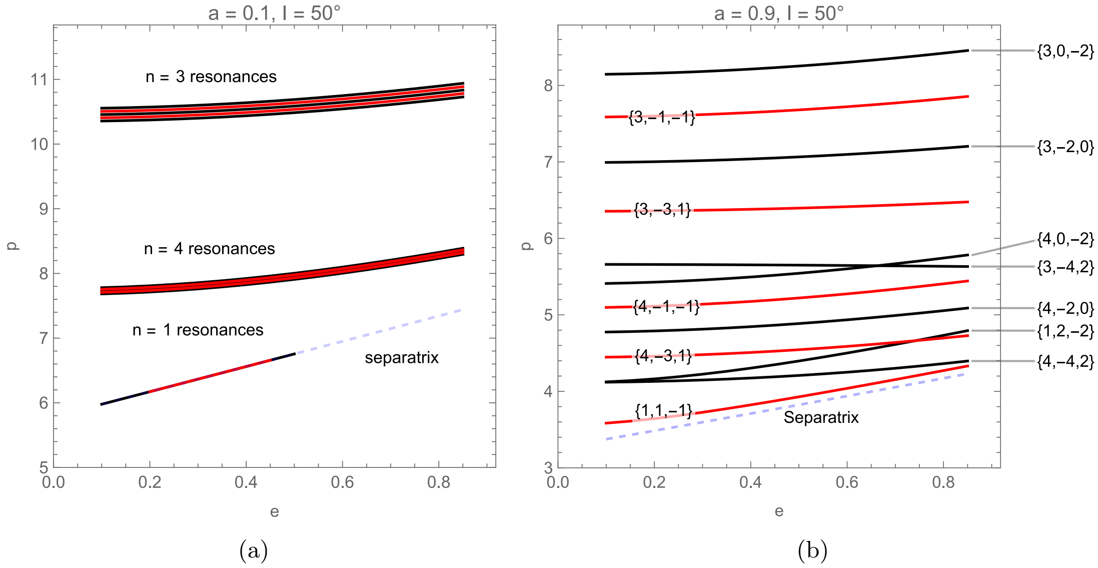

Figure 9: Prograde resonance contours showing the resonant p value as function of e for fixed I. The contour labels correspond to numbers $\{n, k, m\}$. The resonances at $a = 0.1$ are shown in (a) and the resonances at $a = 0.9$ are shown in (b). The blue dashed lines indicate the separatrix.

Note that if the perturber is in the equatorial plane, only the resonances with even m give a nonzero jump in L_z and Q. If the perturber is in a general sky location, all resonances can have an impact on the waveform. Because the tidal force is symmetric in the ϕ-direction when $m = 0$, there is no jump in L_z for $m = 0$ resonances. The jump in Q can be nonzero, so these resonances are still relevant. These resonances happen at the same place as the self force resonances. The only difference between these resonances is the driving force behind the jumps. Distinguishing these resonances from each other requires correct implementation of both types when modeling the waveform.

4.1.2 Dependence on the inclination angle

So far, only the dependence of the resonance contours on a and e has been discussed. However, the position of the resonance contours is also dependent on the inclination angle I. The resonance contours for prograde orbits are shown for different inclination angles ($I = 10°$ and $I = 80°$) in figure 10 (recall, motion in the equatorial plane corresponds to $I = 0°$). The labels (n, k, m) are not shown for clarity. The order of the resonances is the same as in figure 6. It can be seen that the resonance contours shift upwards when I increases. When I increases, ω_θ and ω_ϕ increase and ω_r decreases. Resulting in ω_{nkm} shifting downwards and the resonance contours shifting upwards. The dependence of the orbital frequencies on I is stronger for high a, which is to be expected because, in the Schwarzschild limit, symmetry demands that the results should be independent of the inclination angle.

The (almost) unchanging 'thickness' of the bands in figure 10 shows that the difference between the angular orbital frequencies does not seem to change significantly for varying I. It does seem that the bands themselves slightly move away from each other as I increases, this is likely caused by the changing ratio of ω_r and the angular frequencies.

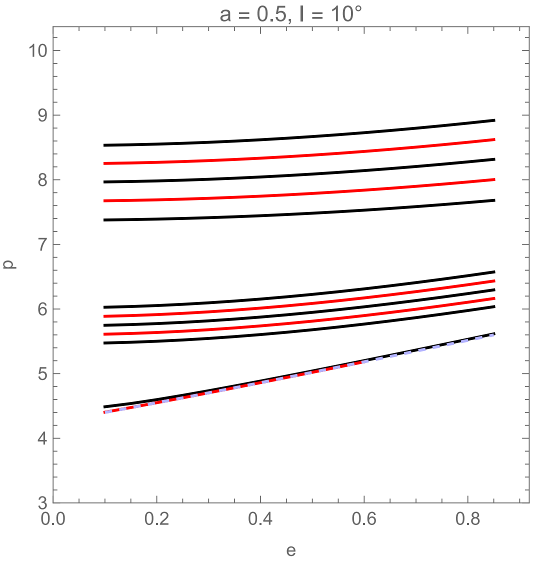

(a)

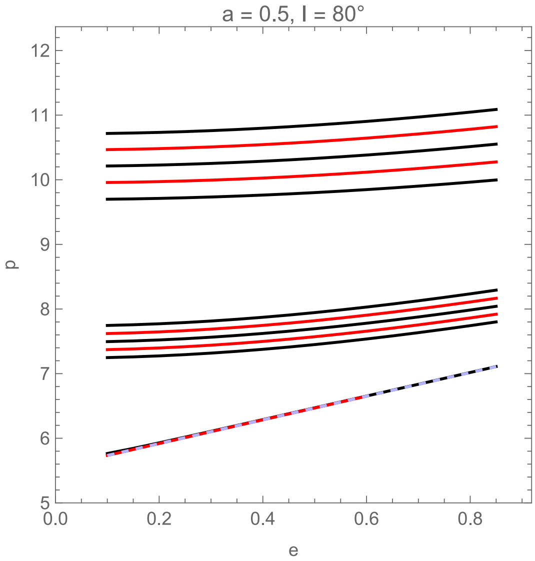

(b)

Figure 10: Prograde resonance contours showing the resonant p value as function of e for fixed a. The order of the resonance contours is the same as in figure 6. The resonances at $I = 10°$ are shown in (a) and the resonances at $I = 80°$ are shown in (b). The blue dashed lines indicate the separatrix.

4.1.3 Retrograde orbits

The above discussion only included prograde orbits. To complete the investigation of the full parameter space, the resonance contours for retrograde orbits will be discussed in this subsection. The retrograde orbits are classified as orbits with $90° < I < 180°$. With this convention, ω_ϕ becomes negative.

The retrograde resonance contours for $a = 0.5$ and $I = 130°$ are shown in figure 11. The black and red contours represent resonances with m even and odd, respectively. It can be seen that the dependence on e is similar to that for prograde orbits. The clustering of the resonance contours with the same n is also visible. The retrograde resonances happen for larger p values compared to the prograde resonances shown in figure 6. This is because the frame-dragging effects are now working against the orbit, resulting in the separatrix and all resonance contours moving to higher p values. If the separatrix is at higher p, the orbital frequencies diverge at a higher p. In figure 12 the values of ω_r, ω_θ and $-\omega_\phi$ are shown as function of p for $a = 0.5$ and $I = 130°$. Here, $-\omega_\phi$ is plotted instead of ω_ϕ for easier comparison with the other frequencies. It can be seen in figure 12 that the functional dependence of the frequencies on p is virtually the same as for the prograde orbits in figure 7, but shifted. Thus, a separatrix at higher p results in a shift of the dependence of the frequencies and, consequently, a shift of the resonance contours to higher p values.

There are two differences in ω_θ and ω_ϕ between prograde and retrograde orbits. First, as mentioned earlier, ω_ϕ is negative for retrograde orbits, while it is positive for prograde orbits. Second, looking at figure 12, it can be seen that $|\omega_\theta| > |\omega_\phi|$ for retrograde orbits, while for prograde or-

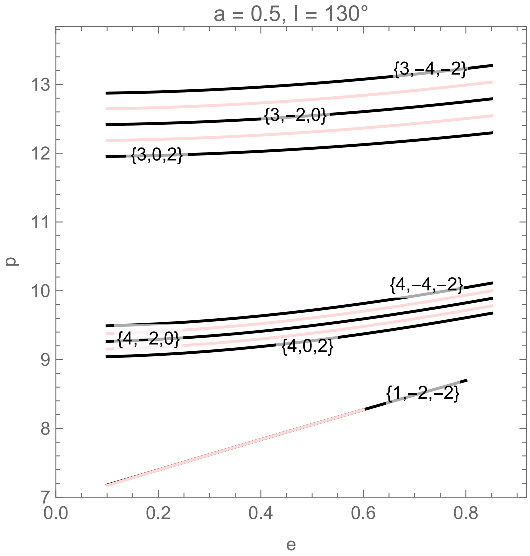

(a)

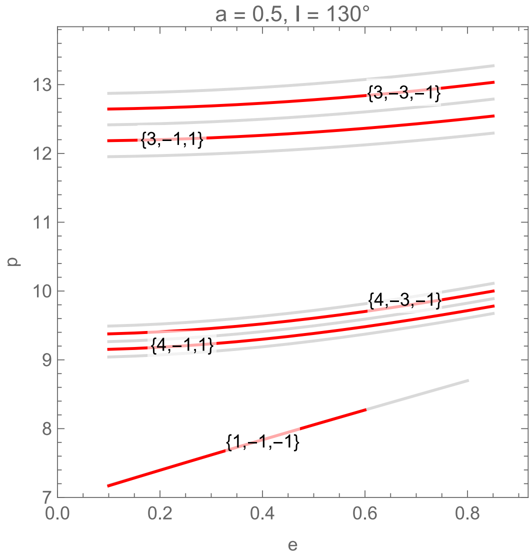

(b)

Figure 11: Retrograde resonance contours showing the resonant p value as function of e for fixed a and I. The resonances with even m are black and labeled in (a) and the resonances with odd m are red and labeled in (b).

bits, $|\omega_\theta| < |\omega_\phi|$. The result of these differences is different for the $n = 1$ resonances compared to the $n = 3$ and $n = 4$ resonances. For the $n = 1$ resonances, having $|\omega_\theta| > |\omega_\phi|$ means that $|\omega_\theta| - |\omega_\phi| > 0$ for retrograde orbits, while it is negative for prograde orbits. Since ω_r is always positive, $|\omega_\theta| - |\omega_\phi|$ must be negative to get a resonance with $|k + m| = 0$. That is why the k and m of retrograde $n = 1$ resonances get a minus sign compared to the prograde combinations. Because ω_ϕ is negative for retrograde orbits, the m gets an extra minus sign. The $n = 1$ resonances thus occur at $(1, -k, m)$ compared to their prograde counterparts. For the $n = 3$ and $n = 4$ resonances, the negative value of ω_ϕ results in the resonances occurring at $(n, k, -m)$ compared to their prograde counterparts. The difference between $|\omega_\theta|$ and $|\omega_\phi|$ only determines the position of the resonance in its band. The result is that the order of the resonances in a band is flipped in comparison to the prograde resonances contours. The resonances $(n,\ 0,\ 2)$ appear now at the lowest p and the resonances with $(n,\ -4,\ -2)$ appear at the highest p.

The retrograde resonance contours for different values of a are shown in figure 13. Figure 13a shows the resonance contours for $a = 0.1$. It can be seen that the retrograde resonances, just like the prograde resonances, group together even more. This is expected behavior because there should be no difference between the resonance contours of prograde and retrograde orbits in the Schwarzschild limit. Thus, the retrograde resonance contours, like the prograde resonance contours, should overlap at $a = 0$. The behavior of the frequencies also explains the grouping of the retrograde orbits. When a goes to zero, ω_θ becomes equal to $-\omega_\phi$. This results in the resonances contours with the same n and $k - m$ being at the same position. The $n = 1$ resonance contours seem to cross the separatrix around $e = 0.3$ in figure 13a. Again, the exact location of this crossing could not be determined because the resonance finder is not precise near the separatrix.

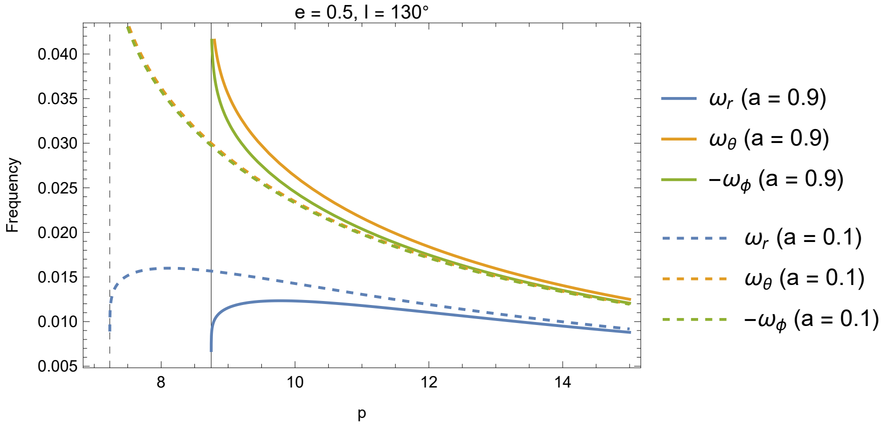

Figure 12: Retrograde frequency plots showing the value of the frequencies as function of p for multiple values of a. The solid lines represent the frequencies at $a = 0.9$ and the dashed lines represent the frequencies at $a = 0.1$. The solid and dashed vertical lines show the location of the separatrix for $a = 0.9$ and $a = 0.1$, respectively.

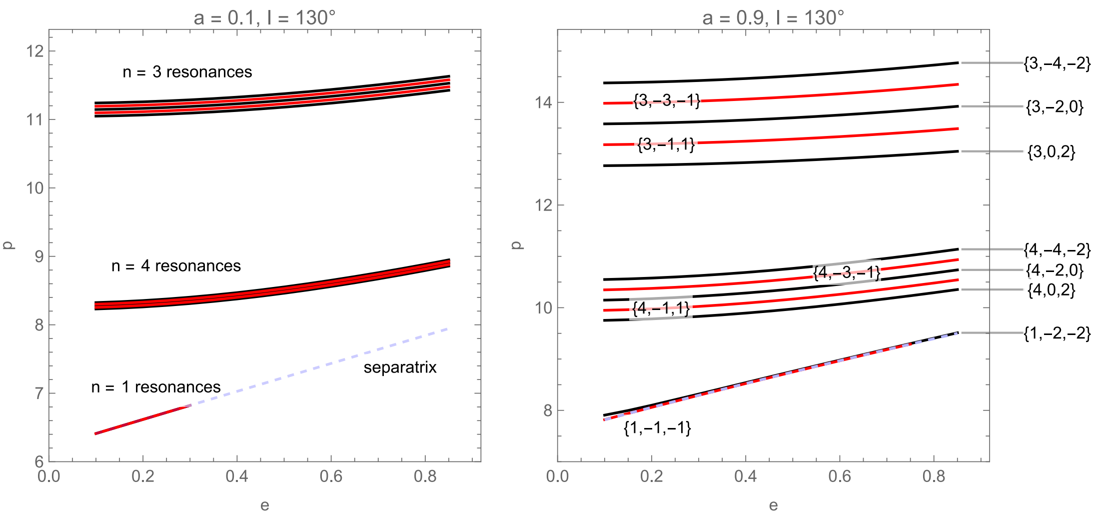

(a) (b)

Figure 13: Retrograde resonance contours showing the resonant p value as function of e for fixed I. The resonances at $a = 0.1$ are shown in (a) and the resonances at $a = 0.9$ are shown in (b). The blue dashed lines indicate the separatrix.

The retrograde resonance contours shown in figure 13b are consistent with the resonances modeled in previous work[16]. It can be seen that the resonances are further apart from each other than for $a = 0.5$, but the bands are still visible. This is a notable difference with the behavior of the prograde resonance contours (see figures 6 and 9) where the bands disappear for high a. The bands seem to remain for the retrograde orbits for two reasons: the resonance contours shift to higher p (instead of lower p for prograde orbits) as a increases, and the contours with a certain n seem to shift apart less with increasing a. The resonances shift to higher p values for retrograde orbits because ω_r decreases while ω_θ and $-\omega_\phi$ increase with increasing a. This causes an overall decrease of the ω_{nkm} and thus a higher p value of the resonance. Why for a given n the contours remain close together despite the high a values is not clear. A possible explanation is that, because the retrograde resonance contours are further away from the central BH, the gravitational effects are weaker, resulting in the contours having more similar behavior and remaining together.

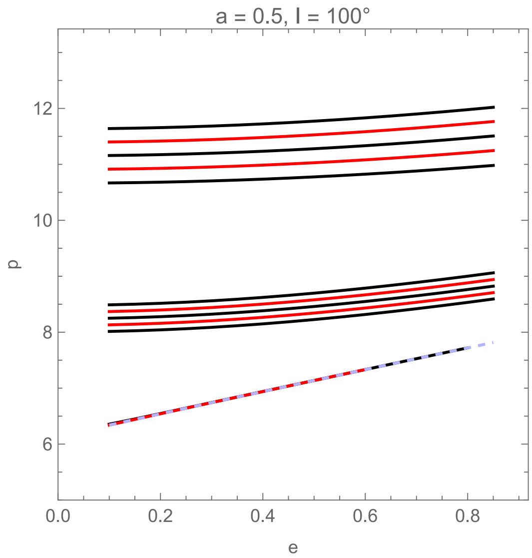

(a)

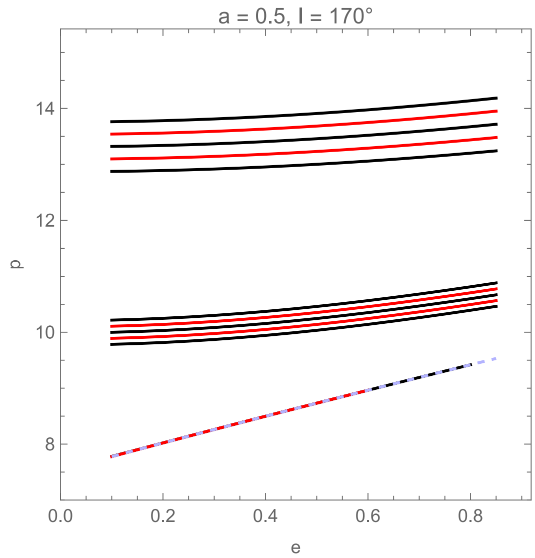

(b)

Figure 14: Retrograde resonance contours showing the resonant p value as function of e for fixed a. The order of the resonance contours is the same as in figure 11. The resonances at $I = 100°$ are shown in (a) and the resonances at $I = 170°$ are shown in (b). The blue dashed lines indicate the separatrix.

The retrograde resonance contours for different values of I are shown in figure 14. It can be seen that the dependence of the retrograde resonance contours on the inclination angle is different from that of the prograde resonances. For prograde orbits (figure 10), the resonances shift to higher p values when moving away from the equatorial plane. For retrograde orbits, the resonances shift to lower p values when moving away from the equatorial plane (i.i. moving away from $I = 180°$). This can be explained by the fact that frame-dragging effects work against the motion of M_2 for retrograde orbits. Resulting in an upward shift of the resonance contours. This effect is the strongest for equatorial orbits and decreases when moving away from the equatorial plane. The resonance contours increase with increasing I for both prograde and retrograde orbits. Note that, for prograde orbits, increasing the inclination angle I is equivalent to moving away from the equatorial plane, and for retrograde orbits, increasing I is equivalent to moving towards the equatorial plane.

4.1.4 Higher n contours

To check if the explanation of the behavior of the orbital frequencies is also consistent with higher n resonances, two $n = 5$ and two $n = 6$ resonance contours are calculated using the resonance finder for both prograde and retrograde orbits. The high n resonance contours for $a = 0.5$ are shown in figure 15. Here, resonances with $n < 5$ are faded and not labeled. Figures 6 and 11 show clearer plots of these $n < 5$ resonances. The location of the $(6, -3, -1)$ resonance in figure 15a can be explained by looking at the n and $k + m$ of this resonance, which is $(n, k + m) = (6, -4) = 2(3, -2)$. This is essentially a resonance with $n = 3$ and $k + m = -2$. Looking at $(n/2,\ k/2,\ m/2) = (3, -1.5, -0.5)$, it is expected that this resonance is located between the $(3,\ -1,\ -1)$ and the $(3,\ -2,\ 0)$ resonances. This is consistent with the position of the $(6,\ -3,\ -1)$ resonance in figure 15a. Keep in mind that resonances can only be looked at in this way to say something about the location of the resonance. In order to study other aspects of the resonance like jump amplitudes or symmetries, the exact (n, k, m) need to be used.

The other three high n resonances in figure 15a have $k + m = -2$ and are located between the $n = 4$ and the $n = 1$ resonances. These resonances occur at low p because $|k+m|$ is low compared to n, so the angular frequencies need to be significantly larger than ω_r for a resonance to take place. This only happens at low p (see figure 7). It is important to note that the order of the resonances displayed by the labels n, k, m in figure 15a is the order of the resonances at $e = 0.85$. The $(6, 0, -2)$ and the $(5, -4, 2)$ resonances intersect for $a = 0.5$ and $I = 50°$. Since only a few $n = 5$ and $n = 6$ resonance contours are modeled, it is expected that more intersections are visible if all resonances with these n values are included.

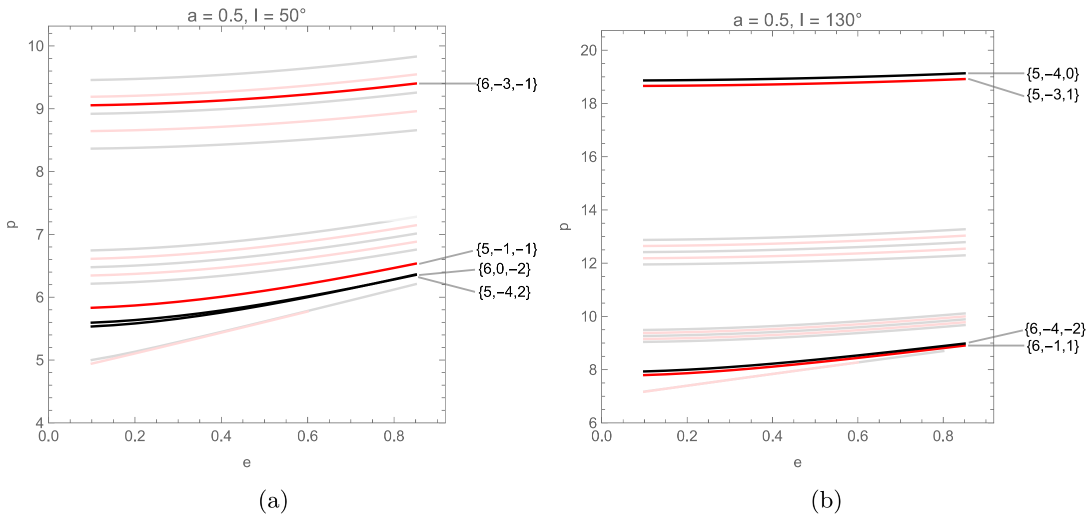

Figure 15: Resonance contours showing the resonant p value as function of e. The $n = 5$ and $n = 6$ resonances are highlighted. Prograde resonances at $a = 0.5$ and $I = 50°$ are shown in (a) and retrograde resonances at $a = 0.5$ and $I = 130°$ are shown in (b).

Figure 15b shows some high n resonance contours for retrograde orbits. The $n = 6$ resonance contours have $k - m = -2$ and are located between the $n = 4$ and the $n = 1$ resonances. It can be seen that the $n = 5$ resonance contours are positioned at very high p compared to the other resonances. This is because the difference between n and $|k - m|$ is relatively small. A smaller relative difference between n and $|k-m|$ means that a resonance occurs when the orbital frequencies are more similar, which happens at higher p. The ratio

$$\rho = \frac{|k \pm m|}{|n|}, \tag{52}$$

where the $+$ is used for prograde resonances and the $-$ is used for the retrograde resonances, can be used as a rough measure of how far the resonance happens from the separatrix. Generally, the closer ρ gets to 1, the higher the p value of the resonance contour. This measure makes use of the approximation that the ω_θ and ω_ϕ frequencies are equal. Meaning that this rule of thumb breaks down at high a.

4.2 Dynamic case

The dynamic case considers all resonances with $-4 \leq n \leq 4$, $-4 \leq k \leq 4$, $-2 \leq m \leq 2$ and $-2 \leq s \leq 2$. Like in the stationary case, it is expected that resonances with higher (n, k, m, s) lead to significantly smaller jumps in the orbital constants. The inclusion of only quadrupolar $l = 2$ moments of the tidal perturbation now constrains m and s to integers between -2 and 2. These initial restrictions on n, k, m and s leave 2025 possible combinations of (n, k, m, s). Most of these combinations do not give a relevant resonance, so these numbers are filtered out as much as possible using the following set of selection rules.

- It has been shown that the tidally induced jumps in L_z and Q are invariant under reflections of the orbit in the equatorial plane [17]. This means that the jumps in L_z and Q are zero unless $k + m + s =$ even, so only resonances with $k + m + s =$ even will be considered.
- If there exists a set of resonance numbers (n, k, m, s), there is a resonance with numbers (jn, jk, jm, js) at the exact same location for any integer j with $|j| > 1$. It is expected that these resonances with (jn, jk, jm, s) are less important since they have higher numbers, so they will be ignored.
- Since (n, k, m, s) and ($-n$, $-k$, $-m$, $-s$) represent the same resonance, we will avoid unnecessary computations by only considering resonances where the first nonzero number is positive.
- For prograde orbits, all orbital frequencies ω_r, ω_θ, ω_ϕ are positive. $\Omega_{\phi,\text{td}}$ is set to a positive value in this thesis.Thus, only sets of numbers with at least one of $k, m, s < 0$ can lead to a resonance.
- For retrograde orbits, ω_r and ω_θ are positive and ω_ϕ is negative. Only sets of numbers with $k < 0$ and/or $m > 0$ and/or $s < 0$ (note the change for m compared to the prograde situation) can thus lead to a resonance.

For the remaining 708 resonance number combinations, a test similar to the rough test in the stationary case should be performed. This test would solve the dynamic resonance condition

$$\omega_{nkms} := n\omega_r + k\omega_\theta + m\omega_\phi + s\Omega_{\phi,\text{td}} = 0. \tag{53}$$

The main difference now is that $\Omega_{\phi,\text{td}}$ is a free parameter, and the dependence of the amount of resonances per (n, k, m, s) on $\Omega_{\phi,\text{td}}$ is non-trivial. Figure 16 shows the sum of the frequencies weighted by their respective integers for $(n, k, m, s) = (3, -1, -1, s)$ and $(3, -3, -1, s)$. The ω_{nkm0} curves correspond to the stationary case. $\Omega_{\phi,\text{td}}$ is independent of (a, p, e, x), which means that the value of s only determines the upward/downward shift of the entire contour. In section 4.1 it was argued that there is no more than one solution to the stationary resonance condition ($s = 0$). In the dynamic case, the curves converge to

$$\varphi_d = (n + k + m)\omega_{\text{kep}} + s\Omega_{\phi,\text{td}} = \varphi_s + s\Omega_{\phi,\text{td}}. \tag{54}$$

This extra freedom allows some (n, k, m, s) to have two solutions to the dynamic resonance condition, depending on the value of $\Omega_{\phi,\text{td}}$. Having multiple solutions requires the ω_{nkms} to have a non-injective dependence on p like the ω_{3-1-1s} curves in figure 16.

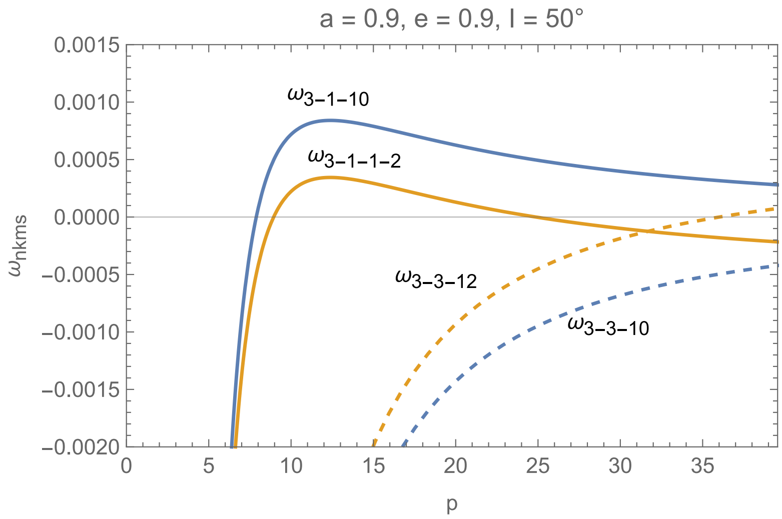

Figure 16: Functional dependence of ω_{3-1-1s} (solid lines) and ω_{3-3-1s} (dashed lines) on p at $a = 0.9$, $e = 0.9$, $I = 50°$ and $\Omega_{\phi,\text{td}} = 2.48159 \times 10^{-4}$.

It can also be seen in figure 16 that the dependence of the ω_{nkms} on p does not always have the same shape. The $(3, -3, -1, 0)$ curve seems to have an injective dependence on p and approaches φ_s for large p. In this case, φ_s is negative, so there is no solution to the stationary resonance condition, meaning that there is no resonance with $(n, k, m) = (3, -3, -1)$ in the static case. It can be seen that ω_{3-3-12} barely crosses zero for $\Omega_{\phi,\text{td}} = 2.48159 \times 10^{-4}$, so in the dynamic case there can be such a resonance depending on the value of $\Omega_{\phi,\text{td}}$. The perturber frequency can realistically be set to values between 5×10^{-5} and 3.5×10^{-4}, so this resonance does not appear in the LISA band for most values of $\Omega_{\phi,\text{td}}$. It may be possible that there are ω_{nkms} that have with a different shape than the ones shown in figure 16. A deeper investigation is required to provide more details, but it is clear from the examples shown in figure 16 that it is not trivial to determine all relevant resonances in the dynamic case. An overview of all relevant dynamic resonances could possibly be obtained from further research by investigating the dependence of ω_{nkm0} of all resonance number combinations that satisfy the selection rules. Developing an accurate and fast way to determine when an orbit is in band would also help to constrain the parameter space for relevant resonances.

Although determining the relevant resonances for all values of $\Omega_{\phi,\text{td}}$ is difficult, determining all relevant resonances for a fixed perturber frequency is quite easy. Some resonance contours were obtained by numerically solving the dynamic resonance condition with $\Omega_{\phi,\text{td}} = 2.48159 \times 10^{-4}$.

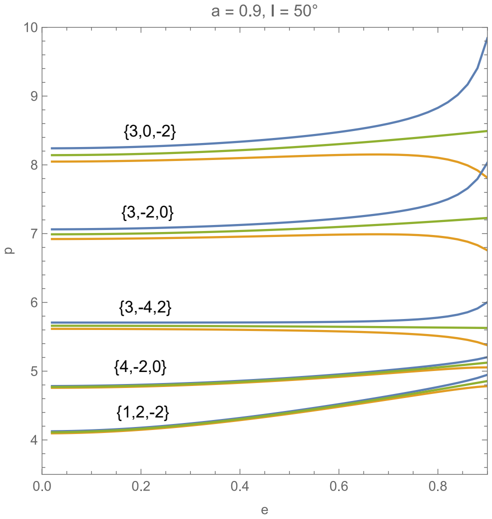

(a) $k + m$ = even, m = even

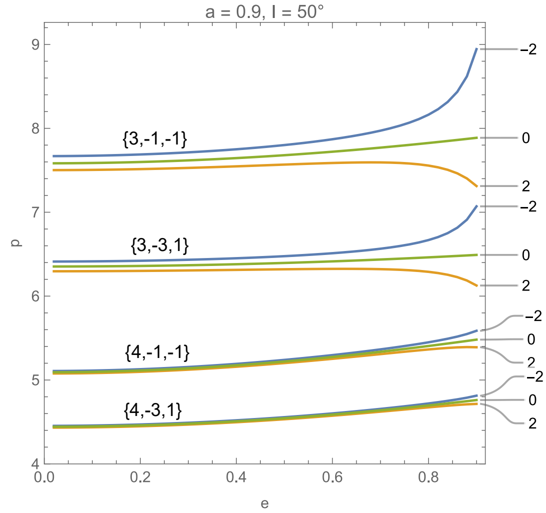

(b) $k + m$ = even, m = odd

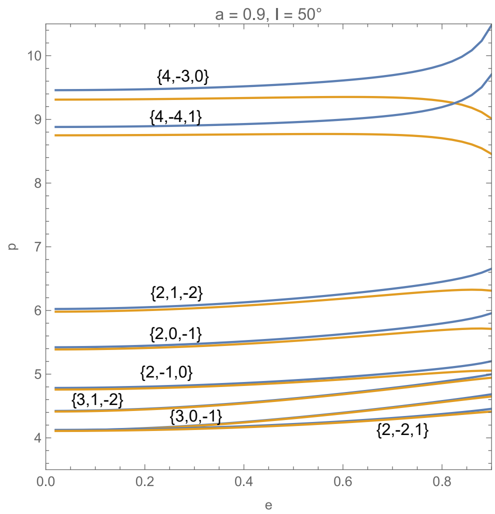

(c) $k + m$ = odd

Figure 17: Dynamic case resonance contours showing the resonant p value as function of e for $a = 0.9$ and $I = 50°$. Resonances with $k+m$ = even and m = even are shown in (a), resonances with $k+m$ = even and m = odd are shown in (b) and resonances with $k+m$ = odd are shown in (c). In (a) and (b), the blue lines correspond to $s = -2$, the green lines correspond to $s = 0$ and the orange lines correspond to $s = 2$. In (c), the blue lines indicate resonances with $s = -1$ and the orange lines indicate resonances with $s = 1$.

The calculated resonance contours are shown in figure 17. Note that the shown resonance contours are likely not all relevant resonance contours.

Figure 17 shows that the addition of the $s\Omega_{\phi,\mathrm{td}}$ term can cause a significant change in the shape of the resonance contours. More research is required to explain the behavior of these changes, especially at high eccentricities, where they appear to grow fast in some cases. It can be seen from figure 17 that the high e behavior of the resonance contours seems to be stronger for higher p resonances. There is also a big difference between the high e behavior of resonances with a different n visible. Explaining these patterns requires more investigation. The high eccentricity behavior of the dynamic case resonances indicate that the frequency of the perturber can have a significant impact on the location of the resonance and thus perhaps also on the jumps. This means that the parameter space may have to be extended to include variations in $\Omega_{\phi,\mathrm{td}}$. If this is done, it is important to investigate the expected dynamics of the perturber to obtain meaningful bounds on $\Omega_{\phi,\mathrm{td}}$.

5 Jump amplitudes

This section covers the results of the calculation of the jump amplitudes for the 24 stationary resonances. Since the dynamic case turned out to be more complicated than expected, no jump amplitudes are shown for the dynamic case. The stationary jump amplitudes are calculated using the code explained in section 3. Note that, due to time translation symmetry, there are no jumps in E in the stationary case. The jump amplitudes in L_z and Q are complex numbers, of which the real part is significantly smaller than the imaginary part. For this reason, the real part of these jumps will be ignored in this discussion.

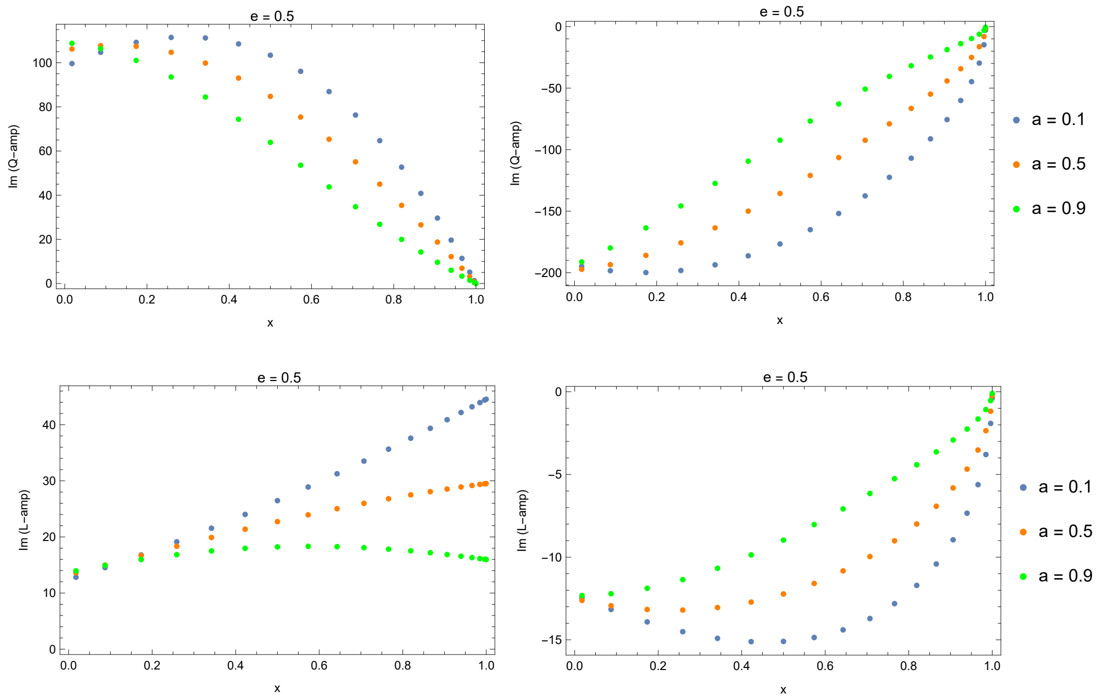

(a) $(n, k, m) = (3, 0, -2)$ (b) $(n, k, m) = (3, -1, -1)$

Figure 18: Imaginary part of the jump amplitudes in L_z (bottom) and Q (top) as function of x for $e = 0.5$ and three values of a. The plots on the left (a) belong to the $(3, 0, -2)$ resonance, and the plots on the right (b) belong to the $(3, -1, -1)$ resonance.

The prograde jump amplitudes of L_z and Q as function of x at $e = 0.5$ belonging to the $(3, 0, -2)$ and $(3, -1, -1)$ resonances are shown in figure 18. The different colors of the dots indicate different values of the central BH spin belonging to the amplitudes. It can be seen from these plots that the shape of the x dependence of the jump amplitudes contains no clear patterns apart from the high x and low x features. As x goes to 1, the jump amplitudes in Q vanish. This behavior is expected and can be explained using the functional form of the rate in Q in Eq. (40). As explained in section 2.4, this rate vanishes for equatorial orbits, meaning that the jumps in Q trivially vanish for $x = \pm 1$. The jump amplitudes in L_z go to zero as well for $x \to 1$ for the $(3, -1, -1)$ resonance, but not for the $(3, 0, -2)$ resonance. The flipped two-for-one deal can be used to explain this difference in behavior. In section 2.4.1, it is explained that this equation relates the jump amplitudes in L_z to the ones in Q whenever $k, m \neq 0$. This means that if $k, m \neq 0$, and the amplitude in Q is zero, the flipped two-for-one deal demands that the jump amplitude in L_z is zero as well. The $(3, 0, -2)$ resonance has $k = 0$ so the flipped two-for-one-deal is not valid for this resonance. This relation is valid for the $(3, -1, -1)$ resonance, and it can be seen that the L_z amplitudes go to zero for equatorial orbits. Note that the jumps in L_z are zero everywhere if $m = 0$ by symmetry.

Figure 18 shows similar behavior of the jump amplitudes in all plots, regardless of the spin value, for high inclination orbits (low x). As $x \to 0$, the dots representing the amplitudes at different a values seem to move toward each other. This behavior is expected as spin effects should become smaller for orbits with a high inclination angle. The jump amplitudes belonging to the $(3, -1, -1)$ resonance seem to almost overlap at $I = 89°$. This is different for the $(3, 0, -2)$ resonance. At very low x, the jump amplitudes in Q become sensitive again to the spin value. The influence of the spin parameter at low x seems to be dependent mostly on k and m. The nature of this dependence is not yet understood. A deeper investigation on these jump amplitudes needs to be performed to provide details on this pattern.

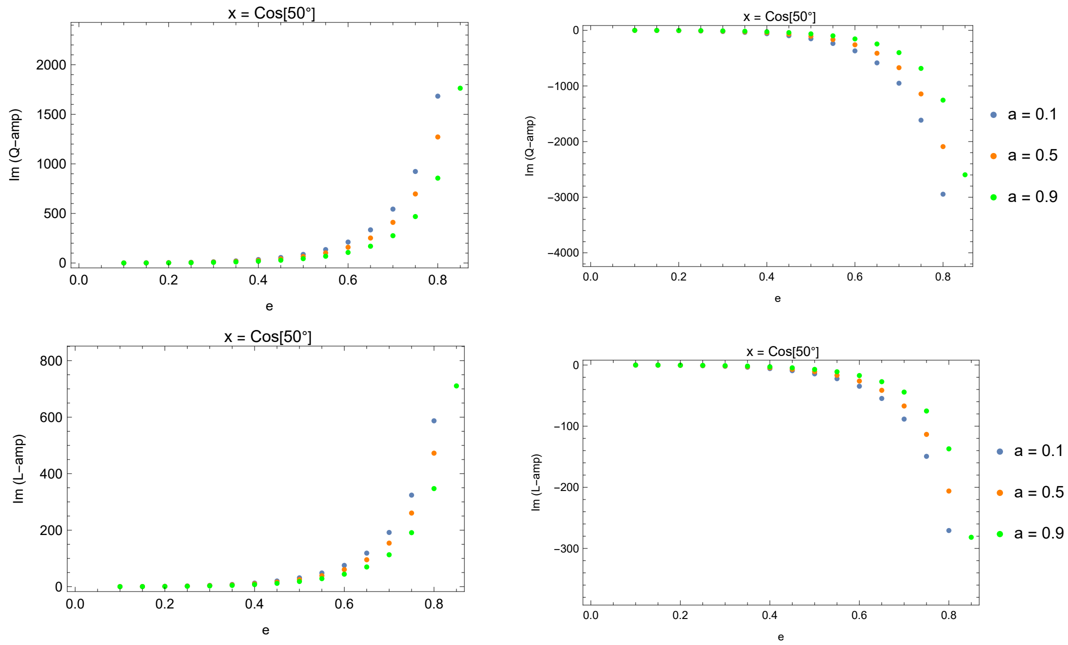

(a) $(n, k, m) = (3, 0, -2)$ (b) $(n, k, m) = (3, -1, -1)$

Figure 19: Imaginary part of the jump amplitudes in L_z (bottom) and Q (top) as function of e for $I = 50°$ and three values of a. The plots on the left (a) belong to the $(3, 0, -2)$ resonance, and the plots on the right (b) belong to the $(3, -1, -1)$ resonance.

Prograde jump amplitudes in L_z and Q are shown as function of e in figure 19. It can be seen in this figure that there is a consistent shape of the dependence of the amplitudes on the eccentricity. This shape shows up for all 24 resonances in the stationary case. The main features of this shape are the steep increase of the jump amplitudes at high e, and the apparent vanishing of the jumps when $e \to 0$. A possible explanation of the high e behavior is that the secondary has a larger apoapsis and a smaller periapsis. Meaning that M_2 comes closer to the perturber and the central BH at higher eccentricities, causing a stronger resonance and thus larger jump amplitudes. Further research has to be done to test this hypothesis. There is no explanation yet for the vanishing of the jump amplitudes for circular orbits. Perhaps there is a symmetry that was overlooked in this research. More research is required to say more about this behavior.

There are only three values of a that the jump amplitudes are calculated for. The low resolution in the a-direction means that plots of the amplitudes as function of the spin parameter do not give much information. However, some observations can be made from figures 18 and 19. First, changes in a don't result in drastic changes in the x dependence of the jump amplitudes of L_z and Q. This helps confirm that the grid size in the a-direction does not need to be large. Second, barring the behavior at very low x for the $(3, 0, -2)$ resonance, the amplitudes belonging to high a are the smallest, and the ones belonging to low a are the largest. This pattern persists for all resonances with $n = 3, 4$. Due to a lack of data, no accurate conclusions can be drawn for the $n = 1$ resonances. More research is required to explain this pattern, and to determine if the pattern is visible for the resonances with $n = 1$.

5.1 Retrograde orbits

The main difference for retrograde orbits compared to prograde is the fact that only negative values of x are considered. The rest of the parameter space remains the same. The dependence of the jump amplitudes on e is very similar to the prograde case. There is again not enough resolution in the a-direction to make meaningful plots, so only plots of the x dependence of the amplitudes will be shown in this subsection. These plots can be found in figure 20.

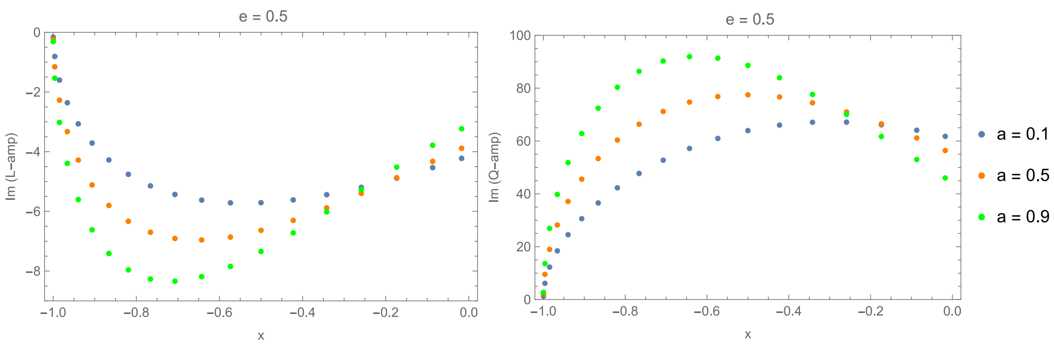

Figure 20: Jump amplitudes in L_z (left) and Q (right) as function of x at $e = 0.5$ for the retrograde $(4, -1, 1)$ resonance. The three colors represent the three values of a belonging to the amplitudes.

It can be seen in the plots that the jump amplitudes go to zero for $x \to -1$, which is to be expected and explained by the same arguments used for the prograde configuration. The influence of a at small x seems to be different compared to the prograde resonances shown in figure 18. Again, more research is required to provide more details on this. Another thing that can be noticed from figure 20 is that the jump amplitudes belonging to the high values of a are now typically the largest, and the amplitudes belonging to the low a values are generally the lowest. This is the opposite of what is observed for prograde resonances. The low x behavior in figure 20 shows that this pattern between high/low a and amplitudes is a trend and not always true. A possible explanation of this trend is that, for prograde orbits, the resonance is closer to M_1 at higher a, meaning that the resonance is weaker. For retrograde orbits the opposite happens. Higher values of the central BH spin result in the resonance occurring further away from M_1 and thus a stronger resonance, thus having larger jump amplitudes.

5.2 Fitting formulas

To obtain a fast and accurate way to estimate the stationary jump amplitudes for every point in the parameter space, the amplitudes at the grid points are fitted with a polynomial in a, e and x. Only the imaginary part is fitted since the real part can be considered negligible. The jump amplitudes belonging to the prograde resonances are fitted with

$$\left\langle \frac{dC}{dt} \right\rangle\Big|_{nkm}(a,e,x) = \frac{e^2}{(1-e)^2}\sum_{i=0}^{N_i}\sum_{j=0}^{N_j}\sum_{l=0/1}^{N_l} C_{ijl}a^i e^j (x-1)^l. \tag{55}$$

The amplitudes induced by retrograde resonances are fitted with

$$\left\langle \frac{dC}{dt} \right\rangle\Big|_{nkm}(a,e,x) = \frac{e^2}{(1-e)^2}\sum_{i=0}^{N_i}\sum_{j=0}^{N_j}\sum_{l=0/1}^{N_l} C_{ijl}a^i e^j (x+1)^l. \tag{56}$$

The prefactor $\frac{e^2}{(1-e)^2}$ in both formulae models for the consistent shape of the e dependence of the jump amplitudes in $C \in \{L_z, Q\}$. Note that (almost) the same function is used to fit the amplitudes in L_z and Q, but the jump amplitudes of the two quantities are fitted separately. The sum over l starts either at 0 or at 1, where 0 is used only for the amplitudes in L_z for resonances where $k = 0$. In all other cases, it is known that the jumps are zero in the equatorial plane for both quantities. That is why the sum in l generally starts at 1, keeping the fitting formula to be zero for equatorial orbits, which is $x = 1$ for prograde resonances and $x = -1$ for retrograde resonances.

The fitting procedure is done in Mathematica, and takes the amplitudes on the grid points as input together with a specified fitting order (N_i, N_j, N_k). The fitting orders used in this project are given in tables 3 and 4 in Appendix B.1. The function NonLinearModelFit is used to find the coefficients C_{ijl}. NonLinearModelFit is used with the 'Method' option set to 'Automatic'. The advantage of using NonLinearModelFit is that it saves fit diagnostics as well. These diagnostics can give information about the accuracy of the fit. Note that the created fitting formula always spans the entire part of the parameter space, regardless of the part where the resonance occurs.

Fitting formulas of the $(3, 0, -2)$ resonance and the $(4, -1, -1)$ resonance are shown in figures 21 and 22, respectively. The respective fitting orders used are (2, 4, 3) and (2, 5, 7) for both L_z and Q. Comparing the plots in the x-direction of both resonances, it can be seen that the fit of the $(3, 0, -2)$ resonance is much better than the fit of the $(4, -1, -1)$ resonance. The latter shows the fitting formula waving through the data points, which is a clear sign of overfitting. It is expected that this resonance would show signs of overfitting first because of the higher fitting order. Overfitting is not necessarily bad for the purpose of this fitting procedure: The fitting formulas cannot be used to extrapolate jump amplitudes for areas far outside the domain covered by the grid. Extreme overfitting can still be an issue, of course. In the case of the $(4, -1, -1)$ resonance, going to lower values of N_j, N_l makes the fit significantly worse. Looking at the dependence of the data and the fit on e for near equatorial orbits, it can be seen that the performance of the fit of the $(4,-1,-1)$ resonance becomes very bad at high eccentricities although note that the jump amplitudes are relatively small here. Related, the performance of the fit in the e-direction gets better for smaller values of x, which is when the jump amplitudes are larger.

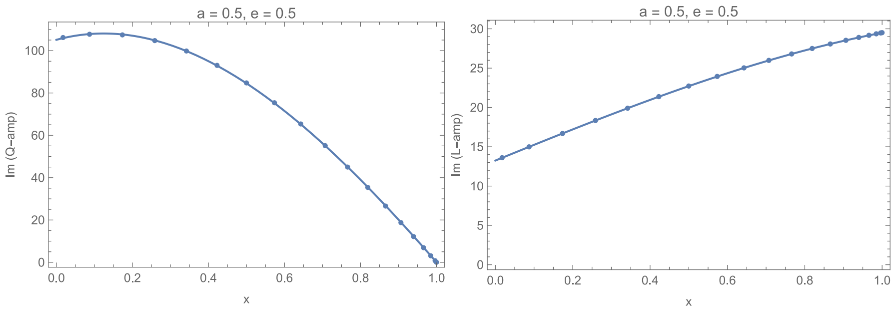

(a) $a = 0.5, e = 0.5$

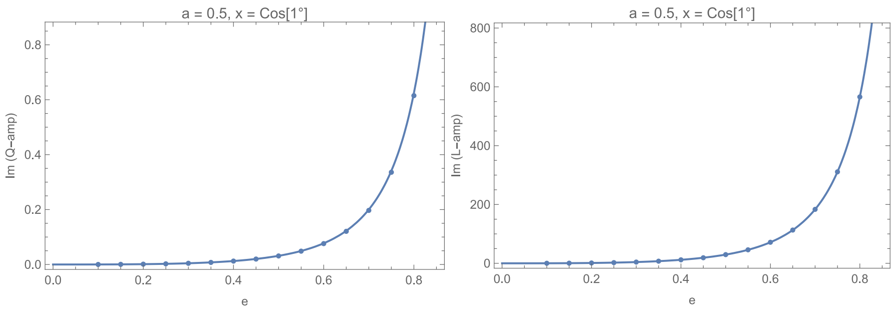

(b) $a = 0.5, I = 1^\circ$

Figure 21: Imaginary part of the jump amplitudes in L_z (right) and Q (left) as function of e (a) and x (b) for the $(3,0,-2)$ resonance. The dots are the data points and the lines represent the corresponding fitting formula.

To better compare the performance of the fits of the two resonances in figures 21 and 22, some diagnostics can be compared. First, the R^2 and adjusted R^2 values can be compared. The R^2 is the coefficient of determination, which measures the fraction of the variability in the data that is explained by the model. R^2 and adjusted R^2 values can range between 0 and 1, where a higher value indicates a larger part of the variance in the dependent variable is explained by the model, meaning a better fit. The difference between the calculation of R^2 and adjusted R^2 is that there is a penalty given for high complexity models with the adjusted R^2 value (in this case, a high fitting order). These values are shown in table 2.

It can be immediately seen that all values of the R^2 and the adjusted R^2 are extremely high. This is unexpected because the fits in figure 22 are not very good. A deeper investigation is required to explain these very high R^2 values. It can also be seen that the values of R^2 and adjusted R^2 belonging to the fitting formula of the $(4,-1,-1)$ resonance are lower than the values belonging to the $(3,0,-2)$ resonances, which is to be expected from the comparison of the plots in figures

(n,k,m)	R^2	Adj. R^2
$(3,0,-2)$	0.999999	0.999999
$(4,-1,-1)$	0.999655	0.99959

(n,k,m)	R^2	Adj. R^2
$(3,0,-2)$	0.999998	0.999997
$(4,-1,-1)$	0.999618	0.999557

Table 2: R^2 and adjusted R^2 values of the fitting formulas of the amplitudes in L_z (left table) and Q (right table) for the $(3,0,-2)$ and $(4,-1,-1)$ resonance.

21 and 22. The adjusted R^2 values in table 2 are only slightly lower than the normal R^2 values, indicating that the fitting orders used for both resonances are not too complex. The difference between these values for the $(4,-1,-1)$ resonance is lower than expected from figure 29. R^2 and adjusted R^2 may not be good metrics to determine the performance of the fitting formulas in this project.

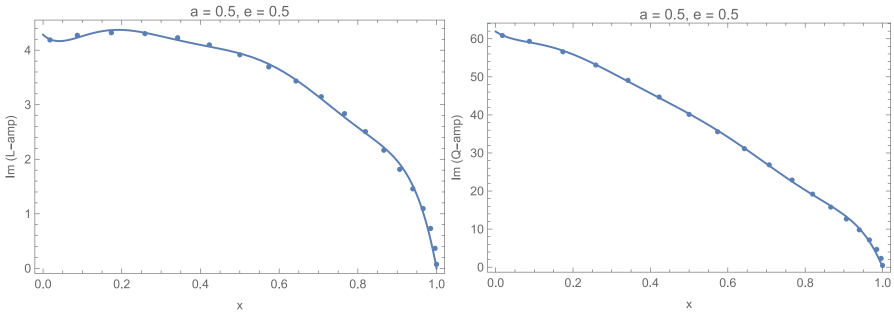

(a) $a = 0.5, e = 0.5$

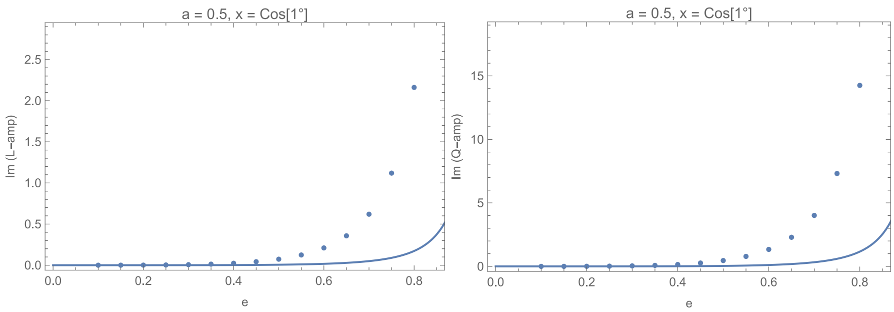

(b) $a = 0.5, I = 1°$

Figure 22: Imaginary part of the jump amplitudes in L_z (left) and Q (right) as function of e (a) and x (b) for the $(4,-1,-1)$ resonance. The dots are the data points and the lines represent the fitting formula.

Another way to check the performance of a model is to look at the residues of the fit. Patterns in the residues might indicate overfitting. Since the jump amplitudes can range over multiple orders, it is more useful to look at the relative residues. The relative residues of the fitting formulas of the Q amplitudes belonging to the $(3,0,-2)$ and the $(4,-1,-1)$ resonance are shown in figure 23. The first thing that can be seen is that the relative residues are practically zero for high e, which is to be expected because the fitting formulas seem to perform best in that part of the parameter space. The only exception is the low x regime for the $(4,-1,-1)$ resonance,

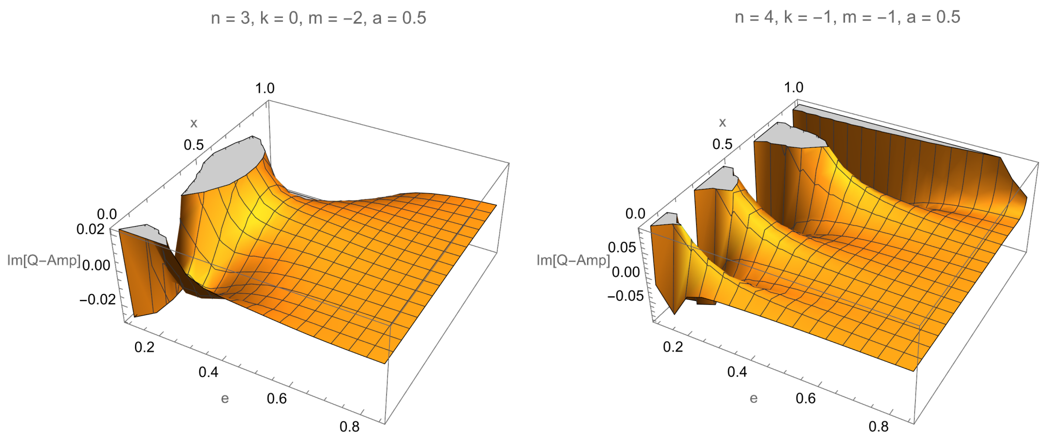

Figure 23: Relative residues of the fits in Q as function of e and x at $a = 0.5$. The left plot represents the residues belonging to the $(3, 0, -2)$ resonance, and the right plot represents the residues belonging to the $(4, -1, -1)$ resonance.

which is where the jumps in Q go to zero. Having a nonzero residue in this situation means that the relative residue will blow up. It is interesting that this doesn't happen for the $(3, 0, -2)$ resonance. Perhaps the residues are very small in this part of the parameter space for this resonance. More research is required to provide details on this.

As e decreases, the relative residues grow, which is expected because the jumps go to zero for $e \to 0$. However, the relative residues only become large at very low eccentricities, which means that both fitting formulas seem to have an error below 5% for most of the parameter space. Looking in the x-direction at low e, it can be seen that both fits in figure 23 show patterns in the residues in the x-direction. This is probably a sign of overfitting. The more oscillating shape belonging to the fitting formula of the $(4, -1, -1)$ resonance indicates a worse case of overfitting for this resonance in the x-direction. Considering the high fitting order in x for this resonance, this is to be expected.

The most problematic areas of the least effective fits are listed and illustrated with plots in Appendix B. It is still a mystery why the fitting procedure has strongly varying results between resonances. It is be possible that the large scale difference in jumps amplitudes in a dataset causes issues for NonLinearModelFit. In that case, a possible way to reduce these issues is to add weights to the data points. Giving data points with small amplitudes higher weights could improve the performance of the fitting formulas in that regime.

6 Summary and outlook

A semi-analytical framework was developed to study the effects of tidal resonances in EMRIs. This method works for EMRIs with either a stationary or dynamic perturbation. In this thesis, a compact mass positioned at a distance significantly greater than the distance between the masses of the EMRI, is considered as the perturbing object. Other forms of tidal perturbations like those induced by an accretion disk or multiple bodies around the EMRI could be studied using the same methods if the metric perturbation can be calculated in these situations. The goal of this thesis was to use this semi-analytical framework to identify the most important resonances, calculate their position in the (a, p, e, x) parameter space and calculate the jump amplitudes induced by these resonances. To do this, a selection of resonance number combinations is made using physical and mathematical arguments. A grid spanning the (a, e, x) parameter space is constructed with the aim to cover as many types of orbits of the secondary as possible. Then, for all these $(n, k, m(, s))$ combinations, the location of the resonance is obtained by solving the resonance condition numerically on the grid. After the determination of the location, the jump amplitudes in the orbital constants E, L_z and Q are calculated.

In the stationary model, 12 resonances are obtained for prograde and retrograde orbits each. For the prograde resonances, the resonances contours show a clear order of resonances in part of the parameter space, and are consistent with previous results[16,17]. At low spin a, the resonance contours group together to form bands. Intersecting resonance contours appeared for prograde orbits with high a. These features at high and low a are hard to model with current codes like FastEMRIWaveforms[13]. Some resonance contours are very close to the separatrix, and appear to cross the separatrix at some point. Due to the inaccuracy of the numerical methods used to solve the resonance condition, the exact location of the crossing points are not known. However, it is expected that these resonances can be ignored because the jumps that are induced by these resonances cannot cause significant dephasing of the gravitational waveform. The resonance contours belonging to retrograde motion show no crossings at high values of the central BH spin. At low a, formation of bands is still visible. Resonances belonging to retrograde orbits occur generally at larger distances between the SMBH and the secondary.

The aim of this thesis was to calculate the location and the induced jump amplitudes belonging to the most important resonances for both the stationary and the dynamic configuration. Throughout this project, it became clear that the dynamic case is significantly more complicated than expected. The extra integer s greatly increases the potential amount of resonances, making the dynamic case significantly more expensive computationally. On top of that, the influence of $\Omega_{\phi,td}$ on the location of a resonance, and thus the influence of $\Omega_{\phi,td}$ on the jump amplitudes, is not trivial. Meaning that the (a, e, x) parameter space potentially has to be expanded to include variations in $\Omega_{\phi,td}$. It was also discovered that it may be possible that the amount of resonances per (n, k, m, s) can depend on $\Omega_{\phi,td}$. At the end of this project, it was discovered that the frequency of the perturber was wrongly implemented into the resonance condition. It is unknown what the impact of this mistake is on the results belonging to the dynamic case in this thesis. The above problems prevented us to identify all relevant resonances, and to calculate their induced jump amplitudes.

Jump amplitudes in L_z and Q are obtained for the 24 resonances belonging to the stationary model. For stationary resonances, the jumps in E are zero by symmetry. The x dependence of the amplitudes in L_z and Q shows that there are no jumps for equatorial orbits, except for resonances with $k = 0, m \neq 0$. Resonances with $k = 0$ and $m \neq 0$ only have nonzero jumps in L_z in the equatorial plane. For all stationary resonances with $n = 3, 4$, the approximate dependence of the jump amplitudes on a is different between prograde and retrograde resonances. For prograde orbits, the jump amplitudes at the highest spin are generally the smallest, while the ones at the lowest a are generally the largest. For retrograde orbits this trend is the other way around: The jump amplitudes at the highest spin are now generally the largest, and the amplitudes with the lowest spin are the smallest. No conclusions can be drawn for $n = 1$ resonances due to a lack of data. The dependence of the jumps on the eccentricity appears to have a very consistent shape. For every resonance, the jump amplitudes grow very fast at high e, and seem to go to zero for $e \to 0$. Confirming these patterns for the resonances with $n = 1$ is difficult due to a lack of data. The shape of the e dependence of the jump amplitudes is not yet understood.

With the aim to obtain fast and accurate estimations of the jump amplitudes for every part of the parameter space, the jump amplitude data is fitted with a polynomial. The performance of the resulting fitting formulas varies a lot between different resonances. For some resonances, a moderately low fitting order is sufficient to obtain a good match of the fitting formula with the data. The fitting procedure seemed to struggle to produce a well performing fit for other resonances. This could be marginally improved by going to high fitting orders, but at the cost of artifacts of overfitting appearing. A potential cause of the low performance of some fitting formulas is the fitting algorithm struggling with the large range of orders of the jumps belonging to a single resonance. This could potentially be solved by adding weights to the data points.

A natural place to start the continuation of this research is the dynamic configuration. The frequency of the perturber needs to be implemented into the resonance condition correctly. Then, all relevant resonances should be identified. It is important for this part that the influence of the perturber's frequency on the amount of resonances is investigated. The locations of the resonances and their jump amplitudes should be obtainable once the resonances have been identified. For both the stationary and the dynamic case, the resonance finder could be improved to make it more robust near the separatrix. This could help get more data on resonances near the separatrix, which would help confirm if they can be ignored or not. A deeper investigation of the stationary jump amplitudes needs to be performed to get more details on the patterns in the amplitudes. This could help improve the fitting procedure, which would improve the estimates of the jump amplitudes from the fitting formulas. The fitting procedure may be improved by using other options like adding weights to the data points or using a different set of basis functions. Finally, the stationary jump amplitudes could be implemented in FEW [13] to start modeling the impact of the resonances on the waveform. A way to deal with banding of and intersecting resonances needs to be developed in order to be able to model multiple resonances into the waveform properly. Hopefully, these new EMRI waveforms can be used to obtain BH parameter estimates from the data gathered by LISA in the future.

References

[1] Rachel Bean, Pedro G. Ferreira, and Andy Taylor. A new golden age: Testing general relativity with cosmology. *Philosophical Transactions of the Royal Society A: Mathematical, Physical and Engineering Sciences*, 369(1957):4941–4946, December 2011.

[2] F. W. Dyson, A. S. Eddington, and C. Davidson. A Determination of the Deflection of Light by the Sun's Gravitational Field, from Observations made at the Total Eclipse of May 29, 1919. *Memoirs of the Royal Astronomical Society, Vol. 62, p. A1*, 62:A1, 1923.

[3] The Event Horizon Telescope Collaboration. First M87 Event Horizon Telescope Results. IV. Imaging the Central Supermassive Black Hole. *The Astrophysical Journal Letters*, 875(1):L4, April 2019.

[4] The LIGO Scientific Collaboration and the Virgo Collaboration. Observation of Gravitational Waves from a Binary Black Hole Merger. *Physical Review Letters*, 116(6):061102, February 2016.

[5] GWTC. The gravitational-wave transient catalog (gwtc). https://gwosc.org/eventapi/html/GWTC/, 2025. Accessed: 28-04-2025.

[6] Christopher J. Moore, Robert H. Cole, and Christopher P. L. Berry. Gravitational-wave sensitivity curves. *Classical and Quantum Gravity*, 32(1):015014, January 2015.

[7] Zhen Pan and Huan Yang. Formation Rate of Extreme Mass Ratio Inspirals in Active Galactic Nuclei. *Physical Review D*, 103(10):103018, May 2021.

[8] Priti Gupta, Béatrice Bonga, Alvin J. K. Chua, and Takahiro Tanaka. Importance of tidal resonances in extreme-mass-ratio inspirals. *Physical Review D*, 104(4):044056, August 2021.

[9] Pau Amaro-Seoane. Relativistic Dynamics and Extreme Mass Ratio Inspirals. *Living Reviews in Relativity*, 21(1):4, December 2018.

[10] Zhen Pan, Zhenwei Lyu, and Huan Yang. Wet Extreme Mass Ratio Inspirals May Be More Common For Spaceborne Gravitational Wave Detection. *Physical Review D*, 104(6):063007, September 2021.

[11] Razieh Emami and Abraham Loeb. Detectability of Gravitational Wave from a population of Inspiralling Black Holes in Milky Way Mass Galaxies. *Monthly Notices of the Royal Astronomical Society*, 502(3):3932–3941, February 2021.

[12] Scott A. Hughes, Steve Drasco, Eanna E. Flanagan, and Joel Franklin. Gravitational radiation reaction and inspiral waveforms in the adiabatic limit. *Physical Review Letters*, 94(22):221101, June 2005.

[13] Fastemriwaveforms. https://github.com/BlackHolePerturbationToolkit/FastEMRIWaveforms.

[14] Saul A. Teukolsky. The Kerr Metric. *Classical and Quantum Gravity*, 32(12):124006, June 2015.

[15] Stephanne Taylor and Eric Poisson. Nonrotating black hole in a post-Newtonian tidal environment. *Physical Review D*, 78(8):084016, October 2008.

[16] Priti Gupta, Lorenzo Speri, Béatrice Bonga, Alvin J. K. Chua, and Takahiro Tanaka. Modeling transient resonances in extreme-mass-ratio inspirals. *Physical Review D*, 106(10):104001, November 2022.

[17] Bart Peters. Tidal resonances in extreme mass ratio inspirals. https://surfdrive.surf.nl/files/index.php/s/dpHByvWQOD8B9GJ?path=%2FGravity, 2023. Accessed: 14-05-2025.

[18] Eric Poisson and Igor Vlasov. Geometry and dynamics of a tidally deformed black hole. *Physical Review D*, 81(2):024029, January 2010.

[19] Eric Poisson. Tidal deformation of a slowly rotating black hole. *Physical Review D*, 91(4):044004, February 2015.

[20] Eric Poisson and Eamonn Corrigan. Nonrotating black hole in a post-Newtonian tidal environment. II. *Physical Review D*, 97(12):124048, June 2018.

[21] Leo C. Stein and Niels Warburton. The location of the last stable orbit in Kerr spacetime. *Physical Review D*, 101(6):064007, March 2020.

[22] Ryuichi Fujita and Wataru Hikida. Analytical solutions of bound timelike geodesic orbits in Kerr spacetime. https://arxiv.org/abs/0906.1420v2, June 2009.

[23] Black hole perturbation toolkit. https://bhptoolkit.org/.

[24] Morteza Kerachian, Lukáš Polcar, Viktor Skoupý, Christos Efthymiopoulos, and Georgios Lukes-Gerakopoulos. Action-Angle formalism for extreme mass ratio inspirals in Kerr spacetime, August 2023.

[25] Wolfram Schmidt. Celestial mechanics in Kerr spacetime. *Classical and Quantum Gravity*, 19(10):2743–2764, May 2002.

[26] Béatrice Bonga, Huan Yang, and Scott A. Hughes. Tidal resonance in extreme mass-ratio inspirals. *Physical Review Letters*, 123(10):101103, September 2019.

[27] Tanja Hinderer and Eanna E. Flanagan. Two timescale analysis of extreme mass ratio inspirals in Kerr. I. Orbital Motion. *Physical Review D*, 78(6):064028, September 2008.

[28] Éanna É. Flanagan and Tanja Hinderer. Transient Resonances in the Inspirals of Point Particles into Black Holes. *Physical Review Letters*, 109(7):071102, August 2012.

[29] Priti Gupta, Takafumi Kakehi, and Takahiro Tanaka. Resonant jumps induced by stationary tidal perturbation: A two-for-one deal. *Classical and Quantum Gravity*, 39(24):245005, December 2022.

[30] B. T. Polyak. Newton's method and its use in optimization. *European Journal of Operational Research*, 181(3):1086–1096, September 2007.

[31] Jeandrew Brink, Marisa Geyer, and Tanja Hinderer. The Astrophysics of Resonant Orbits in the Kerr Metric. *Physical Review D*, 91(8):083001, April 2015.

A Derivation of the flipped two-for-one deal

This derivation is analogous to the derivation of the two-for-one deal in [29]. Details on the approximations and assumptions made can be found there, together with test results on the accuracy of the relation. The jumps in the actions ΔJ_i are approximately related to each other in the following way

$$\Delta J_t(=-\Delta E) : \Delta J_r : \Delta J_\theta : \Delta J_\phi(=\Delta L_z) = \left\langle \frac{dJ_t}{d\tau} \right\rangle : \left\langle \frac{dJ_r}{d\tau} \right\rangle : \left\langle \frac{dJ_\phi}{d\tau} \right\rangle : \left\langle \frac{dJ_\phi}{d\tau} \right\rangle \\ = m\Omega_{\phi,\text{td}} : n : k : m. \quad (57)$$

Note that the : signs indicate proportionality relations (not division). Meaning that if two are compared to each other, the notation can be read as follows

$$\left\langle \frac{dJ_r}{d\tau} \right\rangle : \left\langle \frac{dJ_\phi}{d\tau} \right\rangle = n : m \quad \Leftrightarrow \quad m\left\langle \frac{dJ_r}{d\tau} \right\rangle = n\left\langle \frac{dJ_\phi}{d\tau} \right\rangle. \quad (58)$$

Equation (57) does not work well when $m = 0$, which is when $\Delta L_z = 0$ due to symmetry. To simplify the derivation of the formula for $\frac{dL_z}{d\tau}$ in terms of $\frac{dQ}{d\tau}$, L_z and J_θ are considered to be functions of $\{E, Q, J_r\}$. In this case, the relations

$$1 = \left(\frac{\partial L_z}{\partial L_z}\right)_{E,Q} = \left(\frac{\partial L_z}{\partial J_r}\right)_{E,Q} \left(\frac{\partial J_r}{\partial L_z}\right)_{E,Q}, \quad (59)$$

and

$$0 = \left(\frac{\partial L_z}{\partial Q}\right)_{E,L_z} = \left(\frac{\partial L_z}{\partial J_r}\right)_{E,Q} \left(\frac{\partial J_r}{\partial Q}\right)_{E,L_z} + \left(\frac{\partial L_z}{\partial Q}\right)_{E,J_r}, \quad (60)$$

can be obtained. The subscripts belonging to a derivative indicate the quantities that are being kept constant when taking the derivative. The chain rule can be used to expand the rate in L_z as

$$\frac{dL_z}{d\tau} = \left(\frac{\partial L_z}{\partial J_r}\right)_{E,Q} \frac{dJ_r}{d\tau} + \left(\frac{\partial L_z}{\partial Q}\right)_{E,J_r} \frac{dQ}{d\tau}. \quad (61)$$

In the stationary case, $\frac{dE}{d\tau} = 0$ so that term does not appear in equation (61). Relations (57) and (60) can now be used to rewrite $\frac{dJ_r}{d\tau}$ in terms of $\frac{dL_z}{d\tau}$, and rewrite $\left(\frac{\partial L_z}{\partial Q}\right)_{E,J_r}$

$$\left[1 - \frac{n}{m}\left(\frac{\partial L_z}{\partial J_r}\right)_{E,Q}\right] \frac{dL_z}{d\tau} = -\left(\frac{\partial L_z}{\partial J_r}\right)_{E,Q} \left(\frac{\partial J_r}{\partial Q}\right)_{E,L_z} \frac{dQ}{d\tau}. \quad (62)$$

The terms can be rearranged to get

$$\frac{dL_z}{d\tau} = \left[\frac{n}{m} - \left(\frac{\partial J_r}{\partial L_z}\right)_{E,Q}\right]^{-1} \left(\frac{\partial J_r}{\partial Q}\right)_{E,L_z} \frac{dQ}{d\tau}. \quad (63)$$

Equation (57) can be used again to obtain the expression in terms of J_θ, which is given by

$$\frac{dL_z}{d\tau} = \left[\frac{k}{m} - \left(\frac{\partial J_\theta}{\partial L_z}\right)_{E,Q}\right]^{-1} \left(\frac{\partial J_\theta}{\partial Q}\right)_{E,L_z} \frac{dQ}{d\tau}. \quad (64)$$

The term in front of $\frac{dQ}{d\tau}$ is the exact inverse as the one in equation (25) of[29]. Equation (64) can be written more explicitly as

$$\frac{dL_z}{d\tau} = \frac{K\left[\left(\frac{y_-}{y_+}\right)^2\right]}{\frac{\pi a k}{m}\sqrt{1-E^2}y_+ - 2L_z\left(K\left[\left(\frac{y_-}{y_+}\right)^2\right] - \Pi\left[y_-^2, \left(\frac{y_-}{y_+}\right)^2\right]\right)}\frac{dQ}{d\tau}. \tag{65}$$

B Fitting orders and plots

This section contains the residual information on the fitting formulas in section 5.2.

B.1 Fitting orders

The fitting orders used to create the fitting formulas are given in tables 3 and 4.

(n, k, m)	(N_i, N_j, Nl) for L_z	(N_i, N_j, N_l) for Q
$(1, 1, -1)$	(2, 4, 5)	(2, 4, 6)
$(1, 2, -2)$	(2, 8, 4)	(2, 8, 4)
$(3, -4, 2)$	(2, 4, 6)	(2, 4, 6)
$(3, -3, 1)$	(2, 4, 9)	(2, 4, 9)
$(3, -2, 0)$	*	(2, 4, 4)
$(3, -1, -1)$	(2, 4, 9)	(2, 4, 9)
$(3, 0, -2)$	(2, 4, 3)	(2, 4, 3)
$(4, -4, 2)$	(2, 4, 6)	(2, 4, 6)
$(4, -3, 1)$	(2, 5, 9)	(2, 5, 9)
$(4, -2, 0)$	*	(2, 6, 4)
$(4, -1, -1)$	(2, 5, 7)	(2, 5, 7)
$(4, 0, -2)$	(2, 5, 4)	(2, 5, 4)

Table 3: Fitting orders of the prograde resonances. The * means that there is no fitting formula for L_z because these jumps are zero by symmetry.

(n, k, m)	(N_i, N_j, N_l) for L_z	(N_i, N_j, N_l) for Q
$(1, -1, -1)$	(2, 6, 5)	(2, 6, 5)
$(1, -2, -2)$	(2, 8, 4)	(2, 8, 4)
$(3, -4, -2)$	(2, 4, 6)	(2, 4, 6)
$(3, -3, -1)$	(2, 4, 9)	(2, 4, 9)
$(3, -2, 0)$	*	(2, 4, 3)
$(3, -1, 1)$	(2, 4, 9)	(2, 4, 9)
$(3, 0, 2)$	(2, 5, 4)	(2, 5, 4)
$(4, -4, -2)$	(2, 5, 6)	(2, 5, 6)
$(4, -3, -1)$	(2, 5, 9)	(2, 5, 9)
$(4, -2, 0)$	*	(2, 6, 4)
$(4, -1, 1)$	(2, 5, 9)	(2, 5, 9)
$(4, 0, 2)$	(2, 5, 4)	(2, 5, 4)

Table 4: Fitting orders of the retrograde resonances. The * means that there is no fitting formula for L_z because these jumps are zero by symmetry.

B.2 Plots

Plots showing the remaining main issues from the fitting formulas are shown below.

- $(1, 1, -1)$: Due to this resonance being very close to the separatrix (and going below the separatrix in some areas), the number of data points for this resonance is small. Resulting in fitting formulas that are not accurate throughout the parameter space, but especially at low a and large e, x.

- $(1, 2, -2)$: Similar to $(1, 1, -1)$, this resonance occurs close to the separatrix, resulting in a significant lack of data. This results in the fitting formulas losing accuracy at $a = 0.1$.
- $(3, -1, -1)$: The fitting formulas do not match the data well throughout the parameter space, but especially at $a = 0.1$. When fitting at a high order in x, these issues seem to improve marginally, but at the cost of unwanted behavior of the fit at the edges. This is a sign of overfitting.
- $(4, -4, 2)$: A part of the data is missing at $a = 0.9$. It is expected that this is due to the resonance contour going below the separatrix in this area. The fitting formulas seem to estimate the amplitudes accurately in the rest of the parameter space, however.
- $(4, -3, 1)$: The fitting formulas can't match the data well for almost equatorial orbits, which is when the amplitudes are low. Perhaps this issue can be fixed by introducing weights to the data points.
- $(4, -1, -1)$: This resonance has been covered already in detail in section 5.2, but is listed here for completeness. The fitting formulas show signs of overfitting in the x-direction and can't match the data in the e-direction at x close to 1.
- $(1, -1, -1)$: The resonance contour probably crosses the separatrix, causing big gaps in the data at low a. Resulting in fitting formulas that performs badly across the parameter space, with the worst performance at $a = 0.1$.
- $(1, -2, -2)$: A lack of data at low a, which is likely caused by the resonance contour crossing the separatrix, causes the fitting formulas to perform badly at $a = 0.1$. For the rest of the parameter space, the fits match the data better at high order in e.
- $(3, -3, -1)$: The fitting formulas struggle to match the data in the e-direction at x close to -1. The jump amplitudes are small in this area. Adding weights to the data points might improve the performance of these fitting formulas.
- $(3, -1, 1)$: The performance of the fitting formulas is bad throughout the parameter space, but especially at $a = 0.1$. When fitting at a high order in x, these issues seem to improve marginally, but at the cost of unwanted behavior of the fit at the edges.
- $(4, -3, -1)$: In the e-direction, the fitting formulas can't match the data points for near-equatorial orbits. The jump amplitudes are small in this part of the parameter space.
- $(4, -1, 1)$: The fits in the x-direction don't match the data well across the entire parameter space. At high order in x, the fitting formulas seem to perform a bit better, except at the edges of the parameter space, which is where signs of overfitting appear.

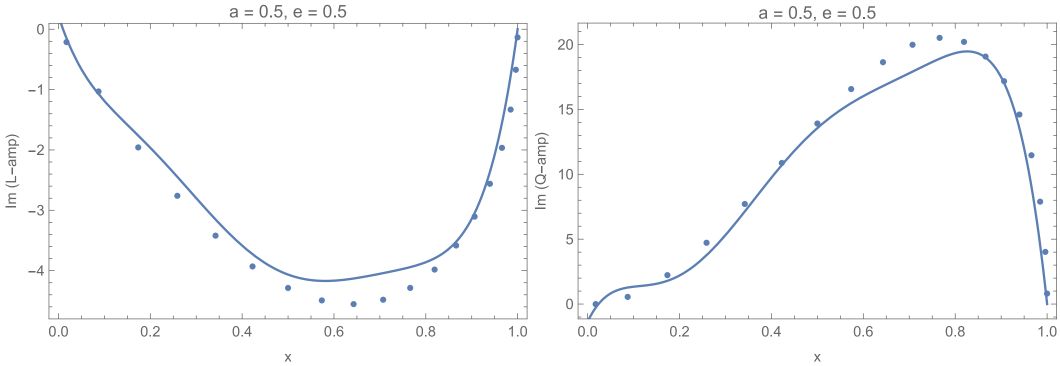

Figure 24: Jump amplitudes in L_z (left) and Q (right) as function of x at $a = 0.5$ and $e = 0.5$ for the $(1, 1, -1)$ resonance. The dots are the data points and the line represents the fitting formula.

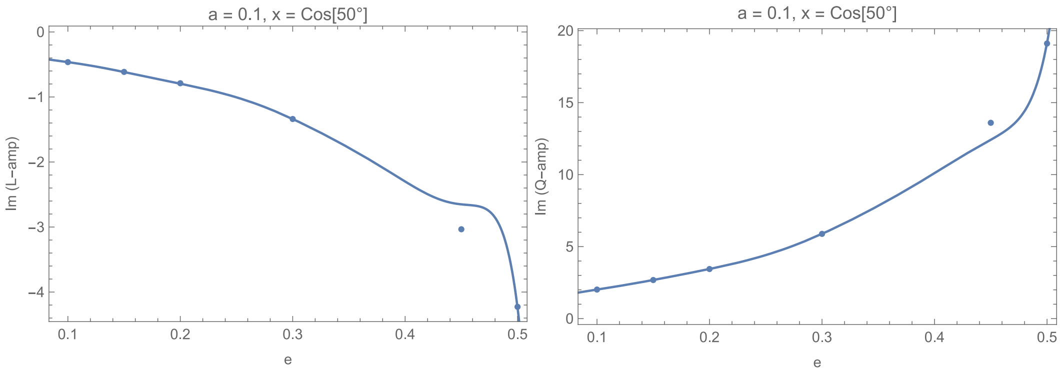

Figure 25: Jump amplitudes in L_z (left) and Q (right) as function of e at $a = 0.1$ and $I = 50°$ for the $(1, 2, -2)$ resonance. The dots are the data points and the line represents the fitting formula.

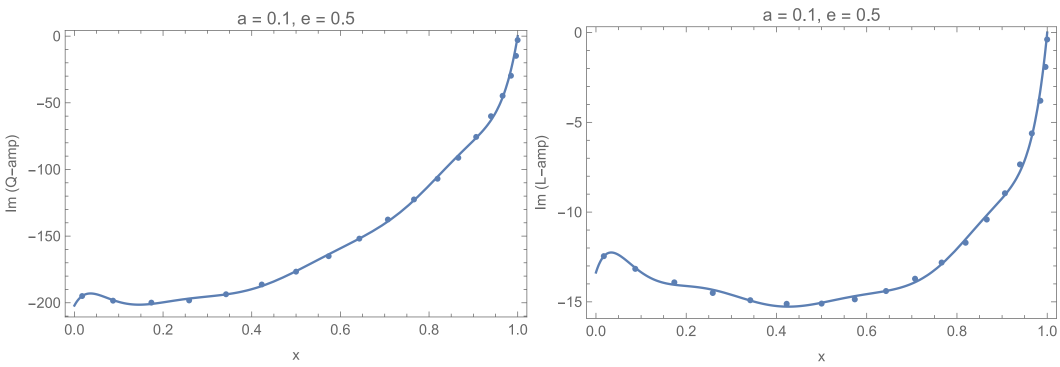

Figure 26: Jump amplitudes in L_z (right) and Q (left) as function of x at $a = 0.1$ and $e = 0.5$ for the $(3, -1, -1)$ resonance. The dots are the data points and the line represents the fitting formula.

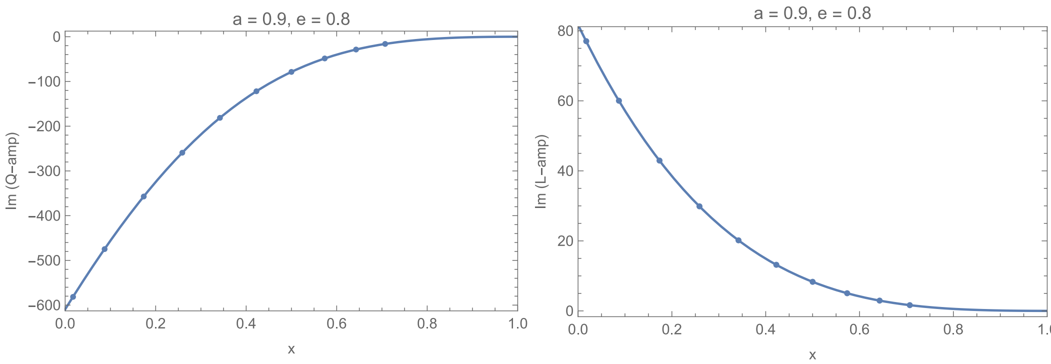

Figure 27: Jump amplitudes in L_z (right) and Q (left) as function of x at $a = 0.9$ and $e = 0.8$ for the $(4, -4, 2)$ resonance. The dots are the data points and the line represents the fitting formula. There are no data points at high e.

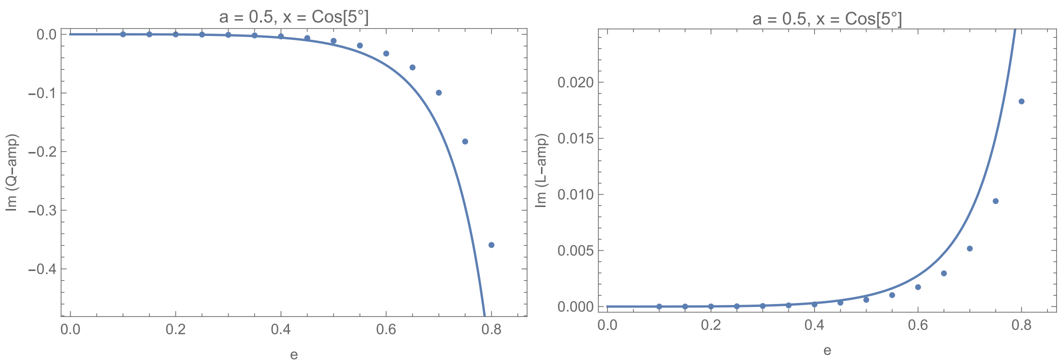

Figure 28: Jump amplitudes in L_z (right) and Q (left) as function of e at $a = 0.5$ and $I = 5°$ for the $(4, -3, 1)$ resonance. The dots are the data points and the line represents the fitting formula. This behavior shows up for near-equatorial orbits ($I \leq 10°$).

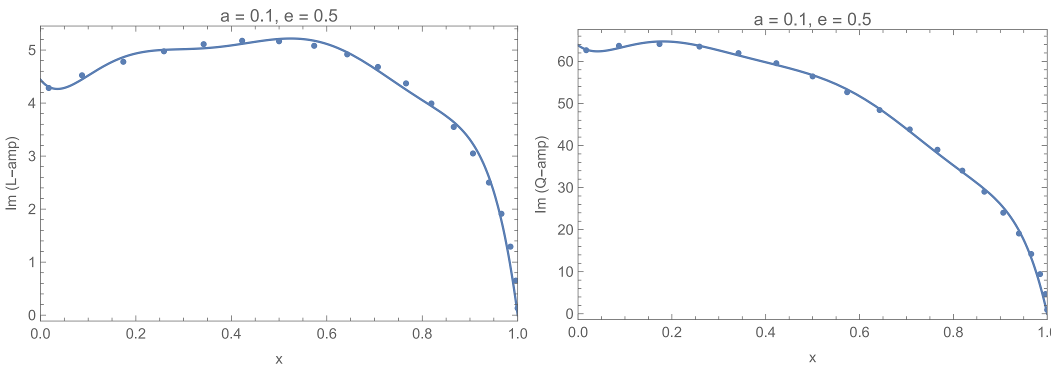

Figure 29: Jump amplitudes in L_z (left) and Q (right) as function of x at $a = 0.1$ and $e = 0.5$ for the $(4, -1, -1)$ resonance. The dots are the data points and the line represents the fitting formula.

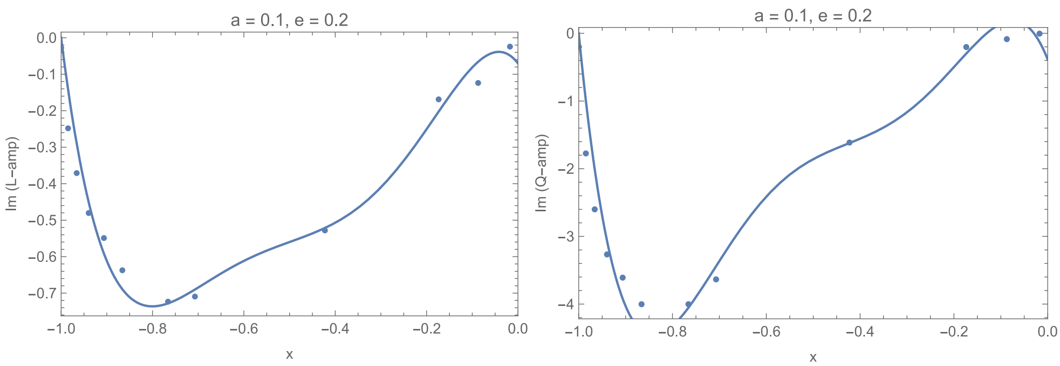

Figure 30: Jump amplitudes in L_z (left) and Q (right) as function of x at $a = 0.1$ and $e = 0.2$ for the $(1, -1, -1)$ resonance. The dots are the data points and the line represents the fitting formula.

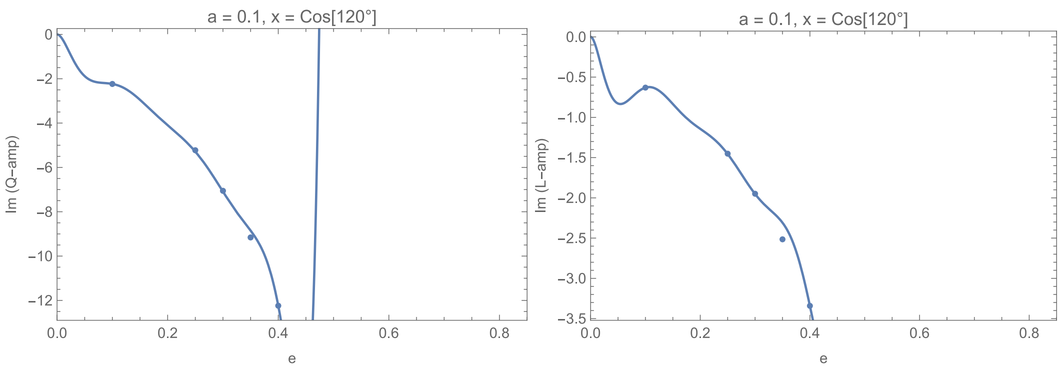

Figure 31: Jump amplitudes in L_z (right) and Q (left) as function of e at $a = 0.1$ and $I = 120°$ for the $(1-2, -2)$ resonance. The dots are the data points and the line represents the fitting formula. The resonance contour crosses the separatrix roughly between e =0.4 and e =0.5. The fast increase of the line in the plot for Q is probably due to overfitting, and outside the part of the parameter space where a resonance occurs, so it should probably be ignored.

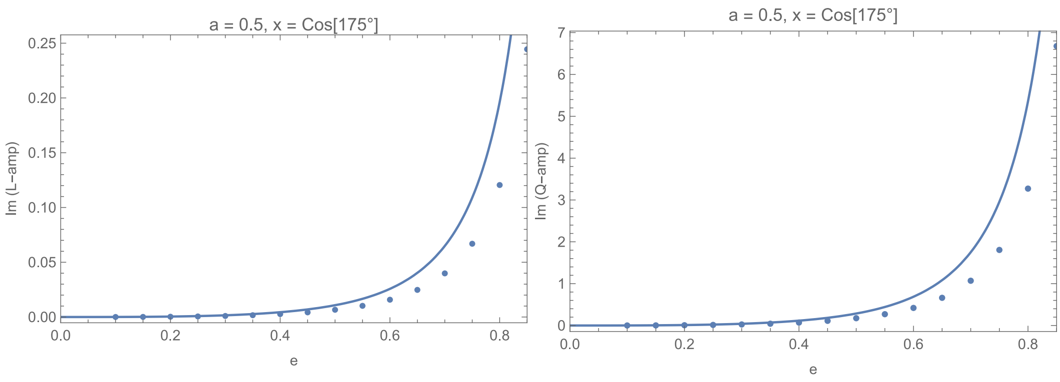

Figure 32: Jump amplitudes in L_z (left) and Q (right) as function of e at $a = 0.5$ and $I = 175°$ for the $(3, -3, -1)$ resonance. The dots are the data points and the line represents the fitting formula. This behavior shows up for near-equatorial orbits ($I \geq 170°$).

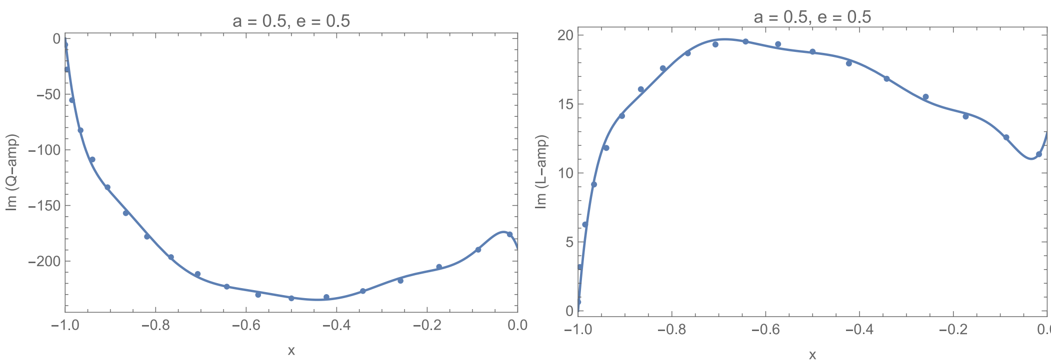

Figure 33: Jump amplitudes in L_z (right) and Q (left) as function of x at $a = 0.5$ and $e = 0.5$ for the $(3, -1, 1)$ resonance. The dots are the data points and the line represents the fitting formula.

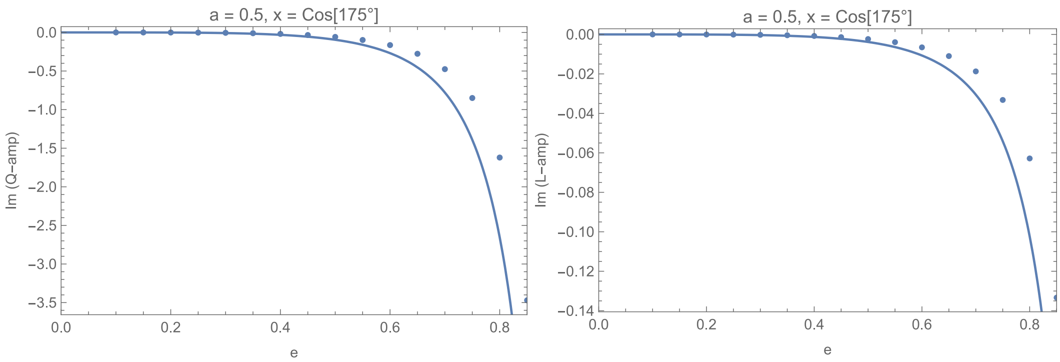

Figure 34: Jump amplitudes in L_z (right) and Q (left) as function of e at $a = 0.5$ and $I = 175°$ for the $(4, -3, -1)$ resonance. The dots are the data points and the line represents the fitting formula. This behavior shows up for near-equatorial orbits ($I \geq 170°$).

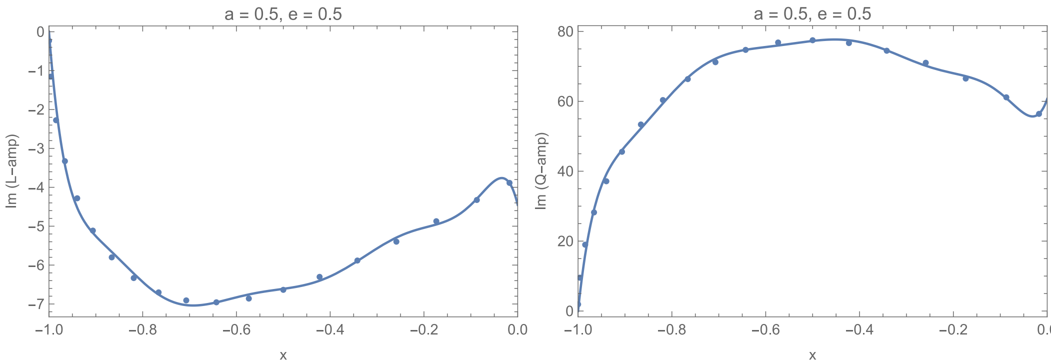

Figure 35: Jump amplitudes in L_z (left) and Q (right) as function of x at $a = 0.5$ and $e = 0.5$ for the $(4, -1, 1)$ resonance. The dots are the data points and the line represents the fitting formula.